RESEARCH ARTICLE

Potential-temperature variance budget in a saturated coastal-fog environment

Francesco Barbano[1,2] | **Eric Pardyjak**[1]

[1]Mechanical Engineering Department, University of Utah, Salt Lake City, Utah, USA

[2]Physics and Astronomy Department, University of Bologna, Bologna, Italy

Correspondence
Francesco Barbano, Mechanical Engineering Department, University of Utah, 1495 E 100 S, Salt Lake City, UT, USA.
Email: francesco.barbano3@unibo.it

Abstract

In this work, we explore the intricacies of the potential-temperature variance budget in coastal fog. We propose an improvement to the theoretical framework of the budget, whereby we include the heat exchange due to water-phase changes. We then show this framework's consistency with a real-world case study from the Coastal Fog (C-FOG) Research Program. Results show that the presence of intermittent energy bursts is driven by the sudden turbulent injection of heat into the environment caused by the condensation of water vapour, and the improved theoretical framework proves satisfactory in detailing the observed process. The heat excess is transported vertically, creating a two-term balance of high-order moments. A bulk parametrization of this balance is also proposed to provide a simplified representation of the phase-change process and suggest that it could be used for operational purposes. Finally, the length-scales of the processes are evaluated from the parametrizations. The analysis indicates that the scales of the phase change of water vapour are consistent with the buoyancy production and Taylor scales.

KEYWORDS

coastal fog, evaporation, saturation processes, surface-layer turbulence, turbulence energy budget

1 | INTRODUCTION

Coastal fog has gained the interest of academics and researchers for over a century. A large effort has been made to study the life cycle of fog, that is, formation, evolution, and dissipation (Nakanishi, 2000), in coastal areas, addressing the physical, microphysical, and chemical processes related to its thermodynamics. Knowing the fog formation mechanism, we can make a first guess regarding the fog type (Gultepe *et al.*, 2007) and evolution (Huang *et al.*, 2015). Lewis *et al.* (2004) identified the main fog

formation mechanisms in warm/cold advection and radiation fog. Advection fog is caused by the thermal contrast between a cold/warm sea surface with respect to the warm/cold (and moist) air above, driving air cooling to saturation by contact/subsidence and mixing. Radiation fog is driven by radiative cooling at the surface when the air temperature meets the dew-point. Other important formation mechanisms are cloud lowering (Koračin *et al.*, 2014) and cloud broadening (Gultepe *et al.*, 2007). The first involves the cloud's descent to the surface causing the reduction of visibility, while the second induces saturation within the

sub-cloud layer, with fog being a separate entity from the cloud but ultimately merging with it.

Fog formation mechanisms are often linked to the characteristics of local turbulence and interactions with the atmosphere aloft. Small-scale turbulence persists within the fog, but changes dramatically according to the phase, playing an important yet not completely understood role. Huang *et al.* (2015) observed that turbulence close to the sea surface can be thermally or mechanically driven, depending on whether the fog forms by cold or warm advection, respectively. This also drives the direction of the sensible and latent heat fluxes upwards in the case of cold advection and downwards with warm advection. Bergot (2013) evidenced the turbulence behaviours in all phases of the fog life cycle: intermittent turbulence kinetic energy (TKE) bursts driving flow stripes during formation, possibly driven by wind shear caused by mean flow or gravity waves aloft the fog layer (Terradellas *et al.*, 2008); upward shift of the TKE maximum (caused by 2D eddies) and very strong scatter on the liquid water content during evolution, leading to 3D turbulence towards the surface; increasing radiative and surface momentum and heat fluxes during dissipation. Inland, fog formation is also delayed by turbulent mixing at the surface, as well as soil temperature and radiative cooling (Maronga & Bosveld, 2017), while latent and sensible heat fluxes tend to balance each other (Terradellas *et al.*, 2008). For radiative and advection fog, vertical mixing in the fog layer due to mechanical production can be generated by increasing wind and wind shear during a mature phase of fog evolution (Dione *et al.*, 2023). Similarly, night-time dissipation can be driven by horizontal advection generating mechanical turbulence, while daytime dissipation also involves solar heating (Dione *et al.*, 2023). For fog events driven by cloud lowering and broadening, the turbulence at the surface is independent of the large-scale dynamics until the cloud invades the surface layer. The lowering of stratus clouds and radiation cooling from its top force cold air and condensed cloud droplets towards the surface (Oliver *et al.*, 1978). The pressure force and mixing below the lowering cloud can cause further condensation of water vapour and further turbulence production (Zhou & Ferrier, 2008). Modelling results from Koračin *et al.* (2005) identified radiative cooling from the top of the cloud-fog layer as a major determinant for turbulence generation inside the cloud-fog. In all cases, mechanical and thermal turbulence is weak compared with a clear-sky day, and it is driven by the thermodynamics of a saturated environment.

Considering the intrinsic heterogeneity of the surface in a coastal area, the operating principles of Monin−Obukhov Similarity Theory (MOST) are not satisfied and the well-known turbulence scalings are disregarded. However, Grachev *et al.* (2018) showed that, apart from the normalized standard deviation of specific humidity, non-dimensional turbulence scalings satisfy MOST reasonably during fog, despite a larger spread in the data distribution owing to the continuous phase changes of water vapour. Phase-change dynamics are always linked with exchanges of latent heat induced by the continuous absorption and release of energy demanded by the saturated atmospheric particles. From a macro-scale perspective, the result of all these energy exchanges is typically negligible, while microscopically it can generate intermittent energy busts or corridors of different mixing ratios with impacts at the turbulence characteristic scales. The latter has been documented by Bergot (2013) and MacDonald *et al.* (2020) as key factors for the evaluation of the TKE budget in the fog layer. Both works identified the impact of heterogeneity within the fog layer as the driver of the TKE imbalance. Bergot (2013) used a large-eddy simulation approach highlighting the formation of three-dimensional rolls in the flow caused by differential heat injection in the layer. Through direct numerical simulation, MacDonald *et al.* (2020) observed the formation of stripes with different densities and thus dynamic characteristics. The intermittent energy burst can be reasonably assumed as a driver of sudden temperature variation, which to the best of our knowledge has never been documented. This major gap in the literature exists largely due to the lack of real-world experimental evidence, as large-scale field campaigns devoted to the detailed characterization of turbulence properties in fog are rare.

To address this gap, we hypothesize that the heat absorbed/released by a saturated particle when its water component changes phase induces a potential temperature change at turbulence length-/time-scales, modifying the potential temperature budget. We investigate the relationship between continuous water-phase change and potential energy bursts within a fog layer, introducing a novel term in the potential-temperature variance budget to better address the turbulence potential energy exchange in a saturated environment. Given the high-order nature of the novel term, we also propose a first-order parametrization of this novel term and the (simplified) budget. The adoption of this updated framework for the potential-temperature variance budget aims to (i) increase the scientific understanding of small-scale turbulence processes regulating fog evolution; (ii) capture, detail, and formalize the physical processes that can occur in a fog layer into an existing mathematical framework, to support the development of better closure schemes for budget equations. This twofold aim steers this study towards researchers in fundamental science to pursue a more exhaustive comprehension of fog evolution. From a broader perspective, the study should lead to improved

parametrization schemes in numerical weather prediction models. Our theoretical framework is tested on a case study from the summer–autumn 2018 field campaign within the Coastal Fog (C-FOG) Research Program (Fernando *et al.*, 2021), a three-year project aiming to improve our knowledge of fog life-cycle processes and fog predictability. The field campaign investigated the coastal areas of the Avalon Peninsula, Newfoundland, Canada, where all fog events occurred under cyclonic systems through cloud lowering and stratus broadening (Dorman *et al.*, 2021).

The article is structured as follows. After this short introduction, Section 2 introduces the modified potential-temperature variance budget used to tackle the research hypothesis. Section 3 describes the case study of this investigation, together with the definition of the preprocessing routine and the method adopted to evaluate the dissipation rate needed for the modified budget; we then describe the spectral analyses and characteristic frequencies that help explain the phase-change process and associated scales of development. Section 4 presents an overview of the mean and turbulence characteristics observed during the fog event, depicting the evolution of the fog layer from formation to dissipation and quantifying key properties of interest that are discussed in Section 5. Section 5 is dedicated to the discussion of the results, starting from the evaluation of the modified potential-temperature variance budget for the entire fog period and the in-depth characterization of the energy peaks through spectral analysis. The second part of the section is devoted to exploring possible bulk parametrizations of this high-order budget. Section 6 summarizes the key conclusions that result from this unique study.

2 | THE POTENTIAL-TEMPERATURE VARIANCE BUDGET IN A SATURATED ENVIRONMENT

The prognostic equation for the potential-temperature variance budget can be written (Hang *et al.*, 2020) as

$$\underbrace{\frac{\partial \overline{\theta'^2}}{\partial t}}_{i} + \underbrace{\overline{u}_j \frac{\partial \overline{\theta'^2}}{\partial x_j}}_{ii} = \underbrace{-2\overline{u'_j \theta'} \frac{\partial \overline{\theta}}{\partial x_j}}_{iii} - \underbrace{\frac{\partial \overline{u'_j \theta'^2}}{\partial x_j}}_{iv}$$
$$- \underbrace{2\epsilon_\theta}_{v} + \underbrace{\frac{2}{\rho C_p} \overline{h'\theta'}}_{vi} + \underbrace{\alpha \nabla^2 \overline{\theta'^2}}_{vii} + \underbrace{\frac{2}{C_p} \overline{\theta'\epsilon}}_{viii}, \quad (1)$$

where each dependent variable is decomposed into a mean component and its stochastic fluctuation (e.g., $u_j = \overline{u}_j +$

u'_j). In Equation (1), t represents time, θ is the potential temperature and $\overline{\theta'^2}$ its variance, $\overline{u}_j$ is the mean wind component in the $j = x, y, z$ direction, u'_j is the wind fluctuation in the j direction, ρ is the mean air density of the layer, $h' = \partial R'/\partial x_j$ is the fluctuation in radiative heating rate, α is the thermal diffusivity of air, C_p is the specific heat of air at constant pressure, ϵ_θ is the potential-temperature dissipation rate, and ϵ is the dissipation rate. Here, terms represent (*i*) potential-temperature variance tendency and (*ii*) advection, (*iii*) turbulence production, (*iv*) turbulence transport, (*v*) thermal dissipation, (*vi*) radiative destruction, (*vii*) molecular dissipation, and (*viii*) dissipation covariance.

In a saturated environment such as fog, the exchange of energy due to the water-vapour phase change can contribute to the potential energy of the environment, as it provides an isotropic injection/subtraction of energy into/from the ambient increasing/decreasing ambient energy (and thus air temperature) at the scale of turbulence. The process is continuous as that of condensation–evaporation, but can generate intermittent energy bursts, leading to sudden ambient temperature increase during the endothermic phase. Being associated with the condensation–evaporation process, this energy supply must be a product of latent heat variation. As such, it is derived as a third-order term from the potential temperature budget, directly from the latent heat flux, which is typically neglected when considering the variance. Possible alternative quantities for a budget investigation of this saturated environment are the liquid water potential temperature and the equivalent potential temperature, but both are conserved for moist adiabatic processes regulating water-phase change. Therefore, the adoption of a non-conserved variable such as the potential temperature is preferred, as it allows us to evaluate the cause of energy exchange.

We considered the complete temperature tendency equation (Cuxart *et al.*, 2015):

$$\underbrace{\frac{\partial \overline{\theta}}{\partial t}}_{i} + \underbrace{\overline{u}_j \frac{\partial \overline{\theta}}{\partial x_j}}_{ii} = \underbrace{-\frac{\partial \overline{u'_j \theta'}}{\partial x_j}}_{iii}$$
$$- \underbrace{\frac{2}{\rho C_p} \overline{h}}_{iv} - \underbrace{\frac{\partial \overline{G}}{\partial x_j}}_{v} + \underbrace{\overline{S}}_{vi} + \underbrace{\overline{B}}_{vii} + \underbrace{\overline{\lambda_E}}_{viii}, \quad (2)$$

where $h = \partial \overline{R}/\partial x_j$ is the radiative heating rate and R is the net radiation, G is the molecular heat flux, S is the storage in the mass elements, B the heat associated with biological processes, and λ_E the latent heat flux. Terms of Equation (2) represent (*i*) potential temperature tendency

and (*ii*) advection, (*iii*) turbulence production, (*iv*) radiation divergence, (*v*) molecular heat flux divergence, (*vi*) heat storage in the ground, (*vii*) biological heat, and (*viii*) latent heat.

Terms (*vi*)–(*viii*) are typically neglected when computing the potential-temperature variance budget as higher-order terms. Nevertheless, we cannot neglect the latent heat flux a priori when we investigate a saturated environment, due to the continuous phase changes that occur at microscopic scales. Therefore, we impose the same manipulation to the latent heat $\overline{\lambda_E}$ as all the other terms of Equation (2) to compute a modified potential-temperature variance budget. Starting from its definition in Cuxart *et al.* (2015), $\overline{\lambda_E}$ is Reynolds decomposed into mean and fluctuation parts, so that

$$
\begin{aligned}
\overline{\lambda_E} &= -\frac{\partial}{\partial x_j}\left(L_v \overline{w'\rho_v'}\right) \\
&= -L_v \frac{\partial}{\partial x_j}\left(\overline{\overline{w'\rho_v'}} + \overline{(w'\rho_v')'}\right) \\
&= -L_v \frac{\partial}{\partial x_j}\overline{w'\rho_v'} - L_v \frac{\partial}{\partial x_j}\overline{(w'\rho_v')'}. \quad (3)
\end{aligned}
$$

The fluctuation component becomes part and is then multiplied by θ' and the result is averaged in time, so that

$$
\begin{aligned}
-L_v \overline{\theta' \frac{\partial}{\partial x_j}(w'\rho_v')'} &= -L_v \frac{\partial}{\partial x_j}\overline{\theta'(w'\rho_v')'} + \overline{(w'\rho_v')' L_v \frac{\partial \theta'}{\partial x_j}} \\
&= -L_v \frac{\partial}{\partial x_j}\overline{\theta'(w'\rho_v')'}, \quad (4)
\end{aligned}
$$

where the divergence of $\overline{\theta'}$ is null, as the fluctuation mean is zero. Inserting the considerations made in Equations (3) and (4) within the formal mathematical procedure to compute Equation (1) from (2) (Stull, 1988), the heat exchange due to the water-vapour phase change would be

$$
-\frac{2L_v}{\rho C_p}\overline{\theta'(w'\rho_v')'}, \quad (5)
$$

which fits into the potential-temperature variance budget as term (*ix*) of Equation (6):

$$
\underbrace{\frac{\partial \overline{\theta'^2}}{\partial t}}_{i} + \underbrace{\overline{u}_j \frac{\partial \overline{\theta'^2}}{\partial x_j}}_{ii} = \underbrace{-2\overline{u_j'\theta'}\frac{\partial \overline{\theta}}{\partial x_j}}_{iii} - \underbrace{\frac{\partial \overline{u_j'\theta'^2}}{\partial x_j}}_{iv} - \underbrace{2\epsilon_\theta}_{v}
$$
$$
+ \underbrace{\frac{2}{\rho C_p}\overline{h'\theta'}}_{vi} + \underbrace{\alpha \nabla^2 \overline{\theta'^2}}_{vii} + \underbrace{\frac{2}{C_p}\overline{\theta'\epsilon}}_{viii} - \underbrace{\frac{2L_v}{\rho C_p}\overline{\theta'(w'\rho_v')'}}_{ix}. \quad (6)
$$

Term (*ix*) is a newly defined term associated with the heat release due to the water-vapour phase change. It accounts

for the endothermic evaporation process cooling the atmospheric layer and the exothermic condensation process warming the atmospheric layer.

3 | DATA AND METHODS

3.1 | A case study from the C-FOG project

The theoretical framework presented in Section 2 is tested using experimental data collected during the C-FOG project (Fernando *et al.*, 2021), which was designed to address the intricacies of the life cycle of fog (formation, persistence, and dissipation) as driven by air–sea–land interactions on the Atlantic coast of Newfoundland, Canada (47.52643°N, 52.65804°W). Specifically, flux-tower data collected at the Battery site are the primary data source for this investigation. Battery is a relatively flat grassy area on the east coast of the Avalon Peninsula. The site instrumentation was located in an almost flat area close to the seashore (about 3 m a.s.l.). Battery was one of the main instrumented areas of the Ferryland supersite, together with The Downs (a promontory with a maximum altitude of 32 m a.s.l. that extends eastwards into the ocean) and supported by the satellite sites of Beach House (21 m a.s.l.) and Judges Hill (129 m a.s.l.) in different inland locations along the slope (see Figure 1). Among other instrumentation equipment not used in this work (Fernando *et al.*, 2021), a 15-m flux tower was equipped with five levels of CSI CSAT-3 sonic anemometers (Campbell Scientific, Logan, Utah, USA) and HMP-155 air temperature and relative humidity sensors (Väisälä, Helsinki, Finland) at 1, 2, 5, 8, and 15 m, respectively. Additionally, two levels of CS EC150 open-path CO_2/H_2O gas analyzers (Campbell Scientific, Logan, Utah, USA) and CGR4 pyrgeometers (Kipp & Zonen, Delft, the Netherlands) at 2 and 15 m were also installed. As ancillary equipment, a visibility sensor PWD52 (Väisälä, Helsinki, Finland) was also used to confirm the presence of fog. Radiosondes were launched approximately every 2 h at The Downs site during the investigation period of this work to profile wind speed and direction, mixing ratio, air and dew-point temperatures, and relative humidity of the whole boundary layer and above. Finally, a ceilometer CL31 (Väisälä, Helsinki, Finland) collected the backscattering of atmospheric particle extinction to detect discontinuity in the vertical atmospheric profile associated with the boundary-layer height or the presence of saturated bodies.

The period investigated within this work covers the tenth Intensive Observational Period (IOP10), which started at 1730 UTC on September 27 and ended at

FIGURE 1 Southern view of Ferryland supersite area with the locations of the subsites: Battery (main site of this investigation), Beach House, Judges Hill, and The Downs. The flux tower, surface energy budget station, ceilometer, and visibility sensors at the Battery site are shown in the right-top panel. [Colour figure can be viewed at wileyonlinelibrary.com]

0330 UTC on September 30 (note that Newfoundland daylight time is UTC − 2.5 h). This period was characterized by patchy fog at the Ferryland shore and low visibility on the ocean for most of the three days under investigation. As we will see in the remainder of this work, a 12-h period of constant fog persisted at Battery during IOP10, thus becoming the focus of the current investigation.

The observed data were run through a preprocessing routine to remove outliers. The first step involves a data check against possible instrument malfunctioning, non-physical data saving, or instrument failure by discarding wind-velocity values larger (in absolute values) than $20\,\mathrm{m\cdot s^{-1}}$, and air and sonic temperatures outside a range of $\pm 40°C$. Data sampled using radiosondes are averaged vertically every 50 m to homogenize the profiles according to the sampling rate, and the mean values are plotted at the midpoint of the averaging depth. The z-averaged values are then linearly interpolated in time to obtain a regular array of measurements in time and elevation. Data sampled using sonic anemometers are further despiked using a data-removal procedure based on Hejstrup (1993), applied to every 30-min data interval (Vickers & Mahrt, 1997).

This procedure assumes that data distribution is Gaussian, with a mean x and a standard deviation σ. Values above the threshold $C\sigma = 3.5\sigma$ (Vickers & Mahrt, 1997) are marked as spikes and replaced with linearly interpolated values within the same 30-min interval. The planar-fit method (Wilczak *et al.*, 2001) is then used to compute turbulence fluxes from the despiked wind components. Notwithstanding the information we intend to extrapolate from the data, a 1-min or 30-min average is applied to the data, intended to verify the dependence of the investigated framework on the averaging time.

3.2 | Spectral analysis and potential-temperature dissipation rate

To delve into the flow characteristics within a saturated environment, power spectra of velocity components and temperature variances, as well as relative vertical covariances, are investigated. A power spectrum of each quantity is computed from sonic-anemometer measurements using the fast-Fourier transform with Hamming windows of 30 minutes and no overlap. Since observations are recorded in time at a fixed location, spectra $S_a(f)$ as a function of frequency f are preferred over $E_a(k)$ in wavenumber k space, assuming $k = 2\pi f/U$ by applying Taylor's hypothesis of frozen turbulence and $fS_a(f) = kE_a(k)$ (Kaimal & Finnigan, 1994).

To evaluate the dissipation rates directly from the power spectra, we identify the inertial subrange within the observed spectra and interpolate it with a common formulation for the streamwise S_u and potential-temperature variance S_θ within the inertial subrange (Barbano *et al.*, 2022). The theoretical spectra in this region are given by

$$S_u(f) = \alpha_K \left(\frac{U}{2\pi}\right)^{2/3} \epsilon^{2/3} f^{-5/3}, \tag{7}$$

$$S_\theta(f) = \beta_K \left(\frac{U}{2\pi}\right)^{2/3} \epsilon_\theta \epsilon^{-1/3} f^{-5/3}, \tag{8}$$

where U is the 30-min averaged wind speed, $\alpha_K = 0.55$ is the Kolmogorov constant, $\beta_K = 0.8$ is the Obukhov–Corrsin constant, ϵ is the dissipation rate of turbulence kinetic energy, and ϵ_θ is the potential-temperature dissipation rate. The frequency range delimiting the inertial subrange is initially guessed using a typical interval (Schiavon *et al.*, 2003). The observed inertial subrange spectra in this range S_a^{in} are then inserted in Equations (7) and (8) to retrieve

$$\epsilon = \left[\frac{S_u^{\text{in}}}{\alpha_{\text{K}} \left(\frac{U}{2\pi} \right)^{2/3} f^{-5/3}} \right]^{3/2}, \tag{9}$$

$$\epsilon_\theta = \left[\frac{S_\theta^{\text{in}}}{\beta_{\text{K}} \left(\frac{U}{2\pi} \right)^{2/3} \epsilon^{-1/3} f^{-5/3}} \right]^{3/2}. \tag{10}$$

To refine the evaluation of the dissipation rates, we deploy an iterative routine: (i) we use the values of ϵ and ϵ_θ obtained in Equations (9) and (10) in Equations (7) and (8) to compute S_u and S_θ; (ii) we compare S_u and S_θ with S_u^{in} and S_θ^{in}, respectively, and compute the respective determination coefficients R^2 of the linear fit; if $R^2 < 0.9$ for both variables we reiterate the computation of S_u^{in} and S_θ^{in}, shifting and subsequently shortening the defining frequency range, compute the dissipation rates once again, and repeat the routine. To prevent testing singularities, the shortening procedure of the frequency range is stopped if there are fewer than four points within the range. If the procedure fails, we attribute a non-value.

To help identify the scale involved in the turbulence phase-change processes, Taylor f_{T}, Ozmidov f_{O}, and Corrsin f_{C} frequency scales, respectively

$$f_{\text{T}} = \sqrt{\frac{\epsilon}{15\nu}} \frac{U}{\sigma_u}, \tag{11}$$

$$f_{\text{O}} = \frac{N^{3/2}}{\epsilon^{1/2}} U, \tag{12}$$

and

$$f_{\text{C}} = \frac{S^{3/2}}{\epsilon^{1/2}} U \tag{13}$$

(where N is the Brunt-Väisälä frequency and $S = dU/dz$) are converted from length- to time-scales adopting Taylor's hypothesis on frozen turbulence, and finally reversed in frequency scales as in Equation (13). These scales will support the spectral analysis and the water-vapour phase-change scale contextualization by fixing the dissipation frequency range (Taylor scale) and marking the separation between buoyancy/shear and inertial subranges (Ozmidov and Corrsin scales).

4 | IOP OVERVIEW

4.1 | Observations on mean and turbulence characteristics of the fog layer

The IOP10 started on September 27, 2018, at 1730 UTC and ended on September 30 at 0330 UTC. The whole period was characterized by an overturning of low-visibility conditions associated with patchy fog, mist, and stratus cloud lowering (Fernando *et al.*, 2021), altering the typical diurnal cycle (Figure 2).

Large oscillations in the wind speed and direction were observed with changing visibility conditions, reducing to an almost wind calm when low visibility became steady. The relative humidity showed saturated or quasi-saturated conditions for most of IOP10, confirming the presence of condensed hydrometeors close to the surface. Consequently, the diurnal variability of air temperature was almost suppressed and a well-mixed environment was established, despite the occasional intensification of the sensible and latent heat fluxes that provided additional energy input, especially closer to the surface. Consistently, TKE remains small during the IOP development, increasing according to the wind speed and the dislodge of saturation conditions. Note that, among the five available sonic-anemometer and thermohygrometer measurement levels along the flux tower, we have used only the 2-m and 15-m levels for the analysis of the energy budget, due to malfunctioning of the anemometers at 5 and 8 m during IOP10 and the location of the 1-m level within the roughness sublayer.

Among the low-visibility events, intense fog occurred between 0000 UTC and 1400 UTC on September 29, with the visibility near the surface continuously below 1 km (Figure 3). The fog bank was observed to cover Battery, Judges Hill, and The Downs, while the Beach House experienced a higher visibility, possibly associated with mist.

Within this period, saturation processes are expected, as relative humidity is close to 100%, while wind speed and turbulence are almost suppressed. Despite an equilibrium being achieved within the fog through atmospheric homogeneity and weak turbulence, mixing and energy variations are present. This is evident in the variance of the air temperature σ_{T}^2 and in the latent heat flux λ_{E}, where intermittent bursts of the same order of magnitude as the rest of the IOP are detected during the whole fog period, despite the TKE remaining small. Latent heat moves into the fog layer through these intermittent events, suggesting their importance for the turbulence budgets despite not being consistent throughout the period. In terms of atmospheric stability, the fog period is mostly under near-neutral conditions, as the atmosphere is forced by small turbulent fluxes, despite periods of stable conditions being observed at the onset of the fog event. Grachev *et al.* (2021) showed that the scaling encompassed by MOST is still applicable within the fog, despite a larger spreading of the data, possibly due to the water-phase transitions and surface heterogeneity. Regarding the energy associated with the phase changes, the heat absorption/release into the environment caused by evaporation/condensation introduces
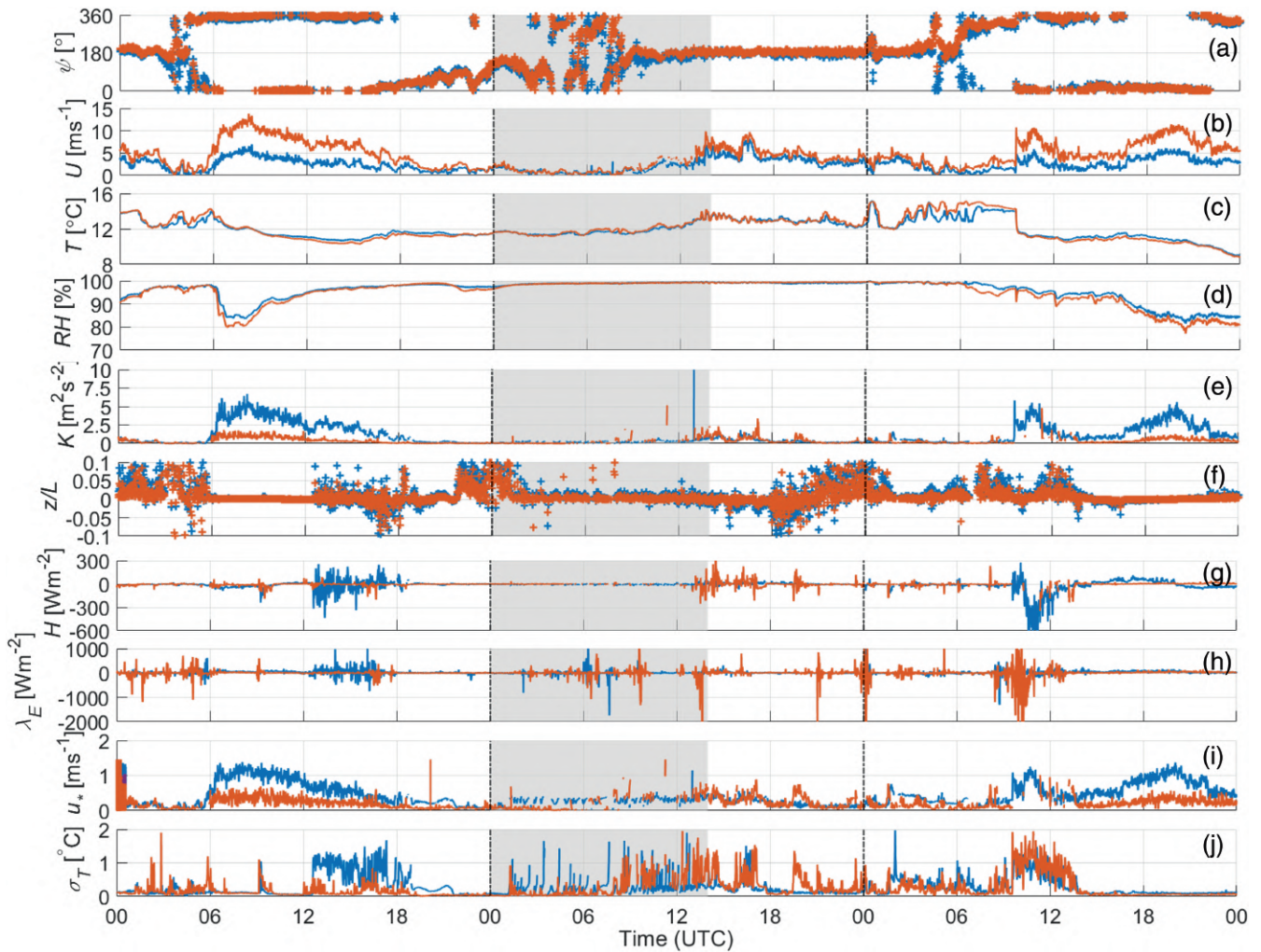
FIGURE 2 Time series of relevant 1-min averaged quantities within IOP10 (from September 28,0000 UTC to September 30, 2359 UTC). From top to bottom: (a) wind direction ψ, (b) wind speed U, (c) air temperature T, (d) relative humidity RH, (e) TKE K, (f) stability parameter z/L (L is the Obukhov length), (g) sensible heat flux H, (h) latent heat flux λ_E, (i) friction velocity u_*, and (l) air temperature variance σ_T^2. Colours identify the measurement level of the flux tower, where blue is 2 m and red is 15 m. The fog sub-period goes from 0000 to 1400 UTC on September 29, and it is highlighted as the grey area. [Colour figure can be viewed at wileyonlinelibrary.com]

additional temperature and humidity fluctuations that lead to deviations from MOST (Grachev *et al.*, 2021). These fluctuations can induce large heat injections that are particularly evident as stability approaches neutrality (Figure 4a), suggesting the existence of some mechanism responsible for intermittent turbulence production.

Note that, despite the temperature scale T_* being small as z/L approaches zero, the heat flux is always a finite value with small oscillations during the fog period. On the other hand, σ_T is still finite but largely fluctuating, causing a sudden increase in the σ_T/T_* ratio. This behaviour of σ_T has already been observed in coastal areas under atmospheric conditions other than fog and is associated with a surface that is thermally heterogeneous and non-uniform in water content causing small-scale advection that enhances σ_T but generally does not affect the surface fluxes, that

is, T_* (Grachev *et al.*, 2018). However, here the values of σ_T/T_* are organized in a coherent structure, strictly following a power-law distribution as a function of z/L (Figure 4b). The coherency of these distributions at both measurement levels suggests the involvement of another heat source within the atmospheric volume; thus the continuous phase heat injection/subtraction is caused by the water-vapour phase change.

Under these near-neutral conditions, a power law is observed following the positive and negative branches of z/L for both measurement levels (Figure 4b), of the form

$$\frac{\sigma_T}{T_*} = a\left(\frac{z}{L}\right)^b. \tag{14}$$

Stability is computed at each layer ($L = L(z)$), and increasing the height of the layer decreases the percentage of
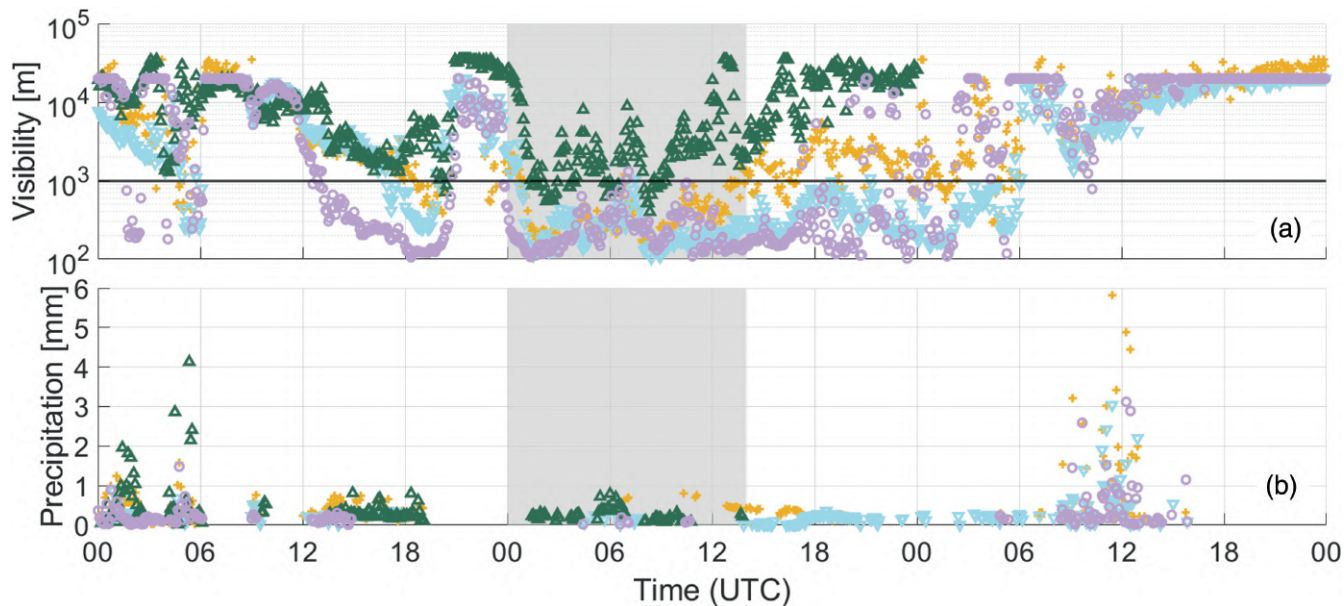
FIGURE 3 Time series of (a) 1-min averaged visibility and (b) precipitation amounts within IOP10 (from September 28, 0000 UTC to September 30, 2359 UTC). Colours and markers identify the sites, namely Battery (orange, plusses), The Downs (light blue, nablas), Beach House (green, triangles), and Judges Hill (violet, circles). The fog sub-period goes from 0000 to 1400 UTC on September 29, and it is highlighted as the grey area. [Colour figure can be viewed at wileyonlinelibrary.com]
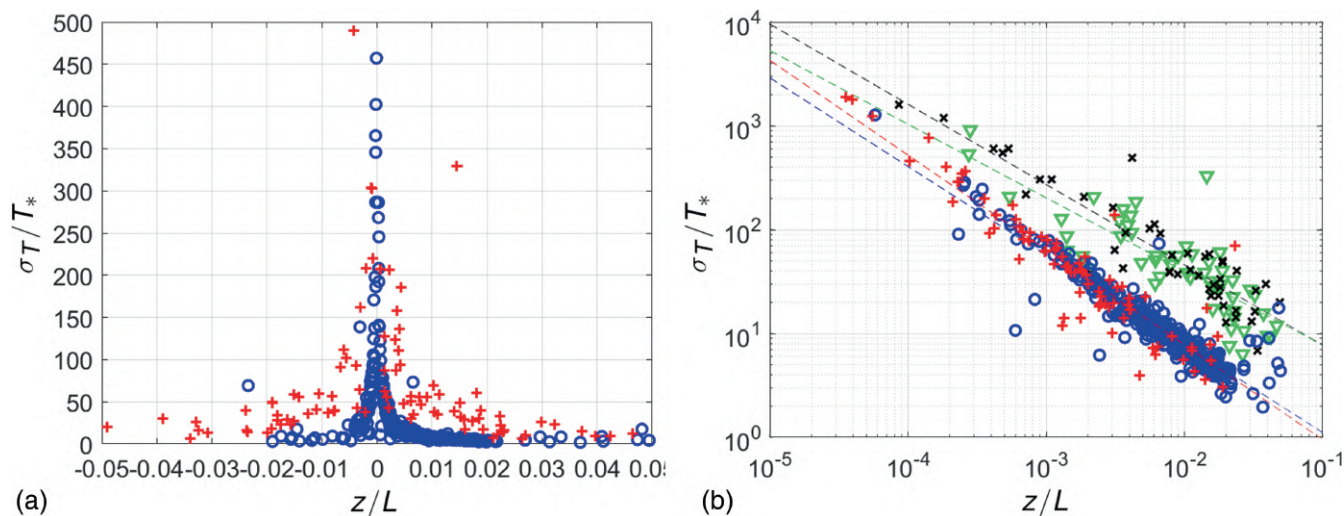
FIGURE 4 Root variance of the air temperature normalized with the temperature scale T_* as a function of the stability ratio z/L, considering near-neutral conditions alone. In (a), the distributions from 2-m (blue) and 15-m (red) datasets are shown. In (b), the 2-m and 15-m distributions are displayed, separating positive and negative branches of the 2-m and 15-m distributions (2-m positive in blue, 2-m negative in red, 15-m positive in green, 15-m negative in black). Logarithmic fits from power laws in Equation (14) follow the respective distribution colours. Data are 1-min averaged and refer to the fog sub-period, 0000–1400 UTC on September 29. [Colour figure can be viewed at wileyonlinelibrary.com]

data falling in near-neutral conditions. Nevertheless, the power laws are similar at 2 and 15 m, with the coefficient $b = [-0.7, -0.9]$. A different slope is instead observed between the 2-m ($a = [0.12, 0.16]$) and 15-m ($a = [1.3, 1.5]$) levels. Values of σ_T/T_* drop within the range $10^{[1,10]}$ as soon as $|z/L| \geq 0.005$ when the anisotropic forcing of the

sensible heat flux (and so T_*) at the surface is sufficient to overcome the isotropic heat input (σ_T). Increasing the distance from the surface, a difference of one/two orders of magnitude persists, as the isotropic heat input remains larger than the forcing from the surface. The positive and negative branches of the curve at the same elevation
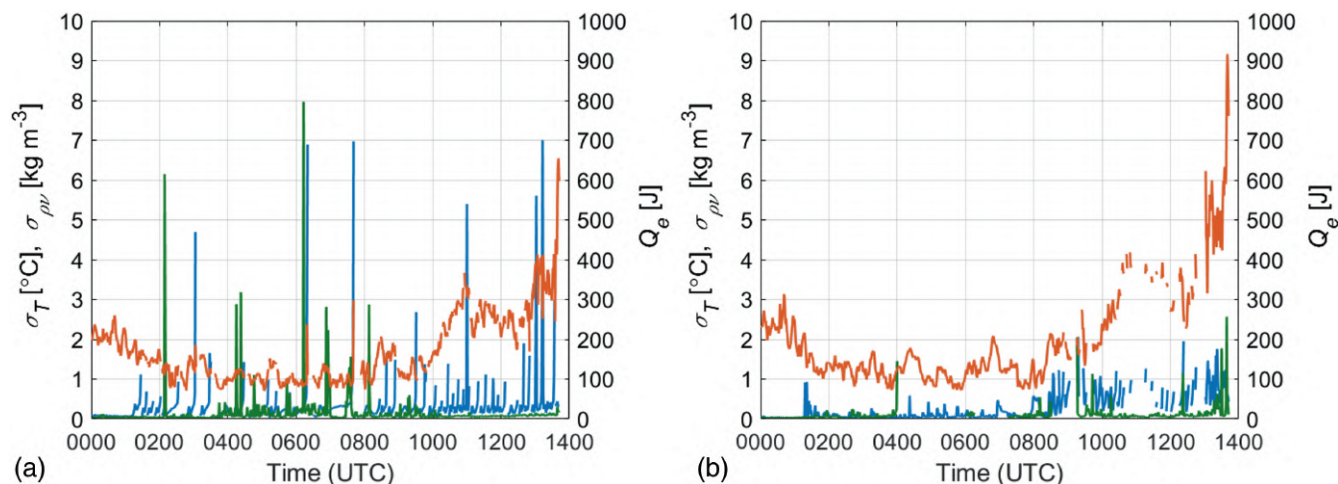
FIGURE 5 Time series of the 1-min averaged evaporation heat loss Q_e (red line, right axis) computed using Equation (15) and compared with the temperature variance σ_T^2 and the water-vapour density variance $\sigma_{\rho_v}^2$ (blue and green lines, respectively, left axis) for (a) 2-m and (b) 15-m measurement levels of the flux tower. [Colour figure can be viewed at wileyonlinelibrary.com]

behave similarly as they approach more unstable and stable conditions, respectively, and do not force a different response in the surface fluxes. The coefficients of determination show the robustness of the applied logarithmic fits based on Equation (14), with R^2 respectively equal to 0.92 for the 2-m positive, 0.97 for the 2-m negative, 0.73 for the 15-m positive, and 0.77 for the 15-m negative branch.

As we have observed so far, peaks in the temperature variance are peculiar characteristics of the fog period. Being a saturated environment, the continuous phase change of water vapour can be responsible for the intermittent release and absorption of energy we observed as peaks in the temperature variance. Impulsive variations in the water-vapour density are indeed observed in the tendency of water-vapour density variance $\sigma_{\rho_v}^2$, which highlights similar peaks to σ_T (see Figure 5). Assuming that a significant part of this density variation is caused by phase-change processes, we can evaluate the water-vapour phase change through the evaporation heat loss, which is a bulk expression to describe the variation of the water-vapour content within a finite volume of air above an evaporating surface. The evaporation heat loss Q_e is computed from an empirical bulk-formulation equation given by Kalogirou (2009) at each flux-tower level as

$$Q_e = (5.64 + 5.96U)(e_s - e), \tag{15}$$

where U is the mean wind speed in m·s^{-1}, e_s (hPa) is the partial pressure of water vapour at saturation computed using the August–Roche–Magnus formula,

$$e_s = 6.1094 e^{(17.625T)/(T+243.04)} \tag{16}$$

(with T the air temperature in °C), and e (hPa) is the water-vapour partial pressure computed considering its link with the specific humidity q:

$$e = p \frac{\frac{q}{1-q}}{\frac{M_v}{M_d} + \frac{q}{1-q}} \tag{17}$$

(with p the total pressure, and M_v and M_d the molar mass of wet and dry air respectively). Compared with σ_T, the evaporation heat loss shows similarities in its intermittency when the sudden energy increase is observed (see Figure 5).

A similar behaviour is found considering the water-vapour density variance $\sigma_{\rho_v}^2$, further linking the energy injection to a variation in the water-vapour density caused by a phase change. The link between these three quantities during intermittent events is stronger at the surface (see Figure 5a), where bursts are clearly observable and detached from the mean behaviour, while decreasing with the elevation (see Figure 5b).

4.2 | Low-tropospheric thermodynamics and fog formation

To investigate fog formation during the study period, we first provide an overview of the lower-tropospheric characteristics by analyzing the ceilometer and radiosonde data shown in Figures 6 and 7, respectively. We focus on a 3000-m depth above the surface, as it encompasses all the atmospheric vertical variability the radiosonde can capture.

The period under analysis involves ~10 h before the fog was detected at Ferryland to capture the formation process. At the synoptic scale, the whole IOP was characterized by a deep polar low to the north and a
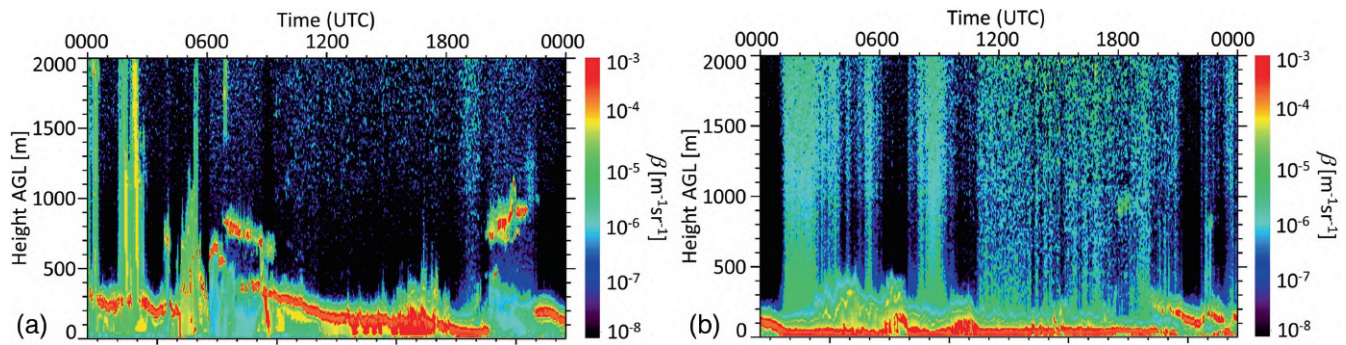
FIGURE 6   Backscatter signal from the ceilometer at Battery for (a) September 28 and (b) September 29. [Colour figure can be viewed at wileyonlinelibrary.com]

tropical cyclone to the south, which caused the long duration and patchy evolution of this fog period and the presence of low stratus clouds (Dorman *et al.*, 2021). Low clouds were detected at 300–400 m above the surface for most of September 28 (Figure 6), descending to lower elevations but rarely becoming fog, since a colder and dryer surface layer (internal boundary layer) sustained stronger winds flowing from the northeast (Figure 7). The fog was only detected between 1730 and 1930 UTC as the stratus cloud finally reached the surface. At 1930 UTC, an intrusion from the southeast of a dryer and faster air mass at 300–900 m (Figure 7a,c) dissipated the cloud–fog system. This forced a flow divergence in the internal boundary layer around 0000 UTC. Starting right after its intrusion and lasting until 0430 UTC, the dry layer rose to above 2000 m, generating a dry cap layer (Figure 7c). During this period, the stratus cloud expanded back over the Avalon Peninsula and a new cloud base appeared at 200 m at 2200 UTC (Figure 6). The cloud base then descended towards the surface and became fog around 0100 UTC (Figure 3).

During the fog period (0100–1300 UTC), a multi-layer structure was observed to evolve during the early stages of the fog formation and persisted until the fog's destruction. A layer between 200 and 1800 m was characterized by increasing wind speed in time and wind rotation from southeast to southwest (Figure 7a,b). This directional transition was guided from the flow at $z > 1800$ m (top-down motion), as the nearly constant warm and saturated cloud stratus descended towards the ground (red area in Figure 7c,d), forcing saturation at the surface (Figure 7e,f). The top-down motion renewed the fog formation at the surface (0–200 m) as soon as the layer was nearly saturated, maintaining it for ~12 h. The cloud layer was topped by the dryer and colder layer at 1800–2700 m, where the lifted air-mass intrusion aligned with the direction of the stratus motion (Figure 7b,d–f). The following three layers stratified the lower troposphere

during the formation and evolution of the fog event under investigation.

- *Fog layer* (0–200 m, decreasing its depth in time): surface layer where the fog is observed, characterized by light landward-directed winds with a top-down cloud motion, forcing an increase in temperature (0400 UTC) and mixing ratio (at 0600 UTC) along with wind-direction rotation (0800 UTC).
- *Stratus-cloud layer* (200–1800 m, developing at 0400 UTC) with increasing wind speed and decreasing air temperature, creating a buffer zone connecting the surface to the atmosphere above.
- *Dry layer* (1800–2700 m, lifting from 600 to 1200 m as it was pushed away from the surface by the previous layer): liquid water content drops to its minimum along the atmospheric column.

Starting at 0800 UTC, a top-down motion of the dry layer caused the mixing and dissipation of the stratus cloud. Recently, top-down motion and associated mixing have been identified as drivers for fog dissipation in other events within the same field campaign (Singh *et al.*, 2023), but it does not seem to be the main driver of this case study. Indeed, as the fog layer started a bottom-up dissipation at Battery (i.e., over land at sea-level height) around 1300 UTC, it persisted longer at the Downs (i.e., over the ocean) and on Judges Hill (i.e., where the elevation delayed the dissipation arrival). As the cloud base lowered to the ground (i.e., when the mixing ratio at the surface reaches the in-cloud values, Figure 7c), the drag force exerted by the land surface on the stratus favoured water condensation, with a slight increase of visibility above the fog threshold of 1 km. Small amounts of precipitation were detected between 1300 and 1800 UTC at Battery, while at Judges Hill and The Downs fog persisted until 1800 and 0600 UTC on 30 September, respectively (Figure 3).
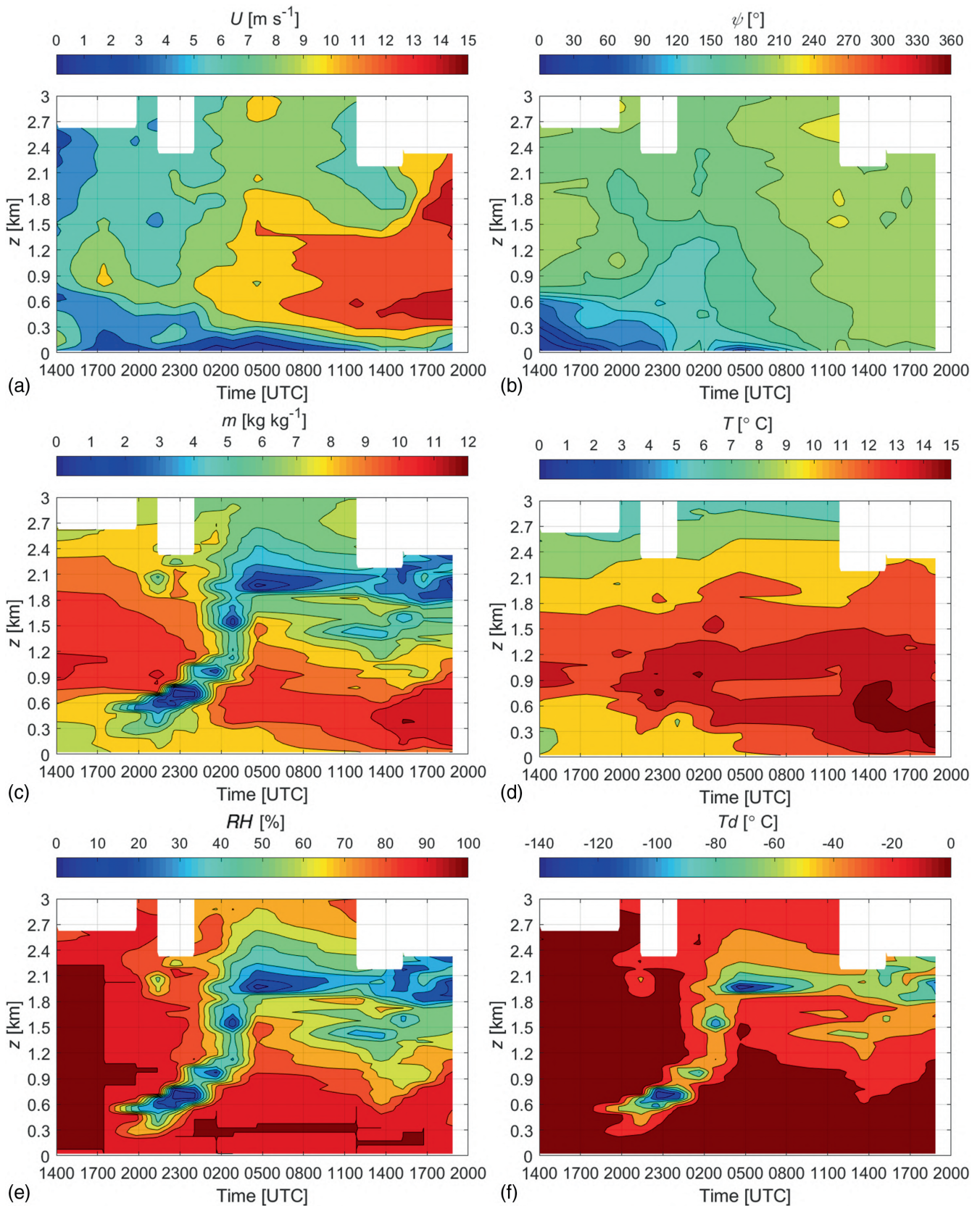
FIGURE 7 50-m averaged and time-interpolated (a) wind speed U, (b) wind direction ψ, (c) mixing ratio m, (d) air temperature T, (e) relative humidity RH, and (f) dew-point temperature Td as measured using the radiosonde at Battery from 1400 UTC on September 28 to 2000 UTC on September 29. The fog sub-period extended from 0000 to 1400 UTC on September 29. [Colour figure can be viewed at wileyonlinelibrary.com]

5 | THE POTENTIAL-TEMPERATURE VARIANCE BUDGET IN THE PRESENCE OF WATER-VAPOUR PHASE CHANGE

5.1 | Surface-layer budget approximation

A budget is performed using a surface-layer approximation of Equation (6) and considering the bulk depth of 2–15 m for the vertical divergence, namely

$$
\underbrace{\frac{d\overline{\theta'^2}}{dt}}_{i} + \underbrace{\overline{u}_j \frac{d\overline{\theta'^2}}{dz}}_{ii} = \underbrace{-2\overline{w'\theta'}\frac{d\overline{\theta}}{dz}}_{iii} - \underbrace{\frac{d}{dz}\overline{w'\theta'^2}}_{iv}
$$

$$
- \underbrace{2\epsilon_\theta}_{v} + \underbrace{\frac{2}{\rho C_p}\overline{h'_z\theta'}}_{vi} + \underbrace{\alpha\nabla^2\overline{\theta'^2}}_{vii} + \underbrace{\frac{2}{C_p}\overline{\theta'\epsilon}}_{viii}
$$

$$
- \underbrace{\frac{2L_v}{\rho C_p}\overline{\theta'\left(w'\rho'_v\right)'}}_{ix}, \tag{18}
$$

where $h'_z = dR'/dz$. The approximation involves discarding the horizontal gradients, forcing the computation to be independent of the advection. Although strong in this work's context, this approximation is forced by the experimental design, which favours computing vertical variations rather than horizontal ones (as typical). It is worth mentioning that an attempt to estimate horizontal advection was made using data from Judges Hill, The Downs, and Beach House (being representative of the inland, ocean, and north–south advection, respectively), but the resulting contributions were negligible.

After computing all terms in Equation (18), Figure 8 shows the time series of each budget term within the bulk fog layer observed by the flux tower.

Energy peaks dominate the time series, describing sudden energy variations (which are evident using 1-min averages, not shown) that are strong enough to preserve their peaks even using 30-min averages. The peaks indicate a balance between the temperature variance turbulent transport and the phase-change term or the turbulent production, with a non-negligible contribution from residuals, possibly due to advection. However, one can argue that advection does not play a major role, as the energy transfer is instantaneous; in other words, until the time-scale of turbulent advection is larger than the other three terms of the budget, the entire energy exchange occurs in a control volume smaller than that of horizontal transport, and the whole process is captured to a reasonable approximation. As expected, several terms are negligible, including molecular dissipation and the dissipation covariances, which are expected to be small in a turbulent flow, as well as radiative
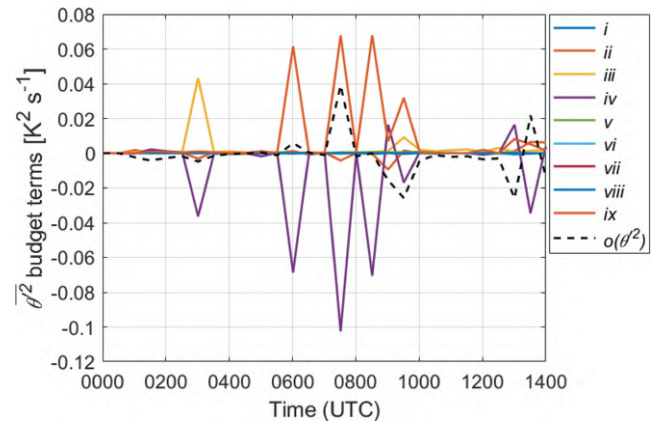

FIGURE 8 Terms of the potential-temperature variance budget in the surface-layer approximation as a function of time for the fog period only. Terms are shown as 30-min averages. Solid lines refer to terms from Equation (18), specifically (*i*) tendency, (*ii*) vertical advection, (*iii*) turbulence production, (*iv*) turbulent transport, (*v*) dissipation, (*vi*) radiative destruction, (*vii*) molecular dissipation, (*viii*) dissipation covariance, (*ix*) water-vapour phase change, and residuals ($\mathcal{O}(\theta'^2)$). [Colour figure can be viewed at wileyonlinelibrary.com]

destruction, as radiation diffuses homogeneously within the fog layer. Dissipation also seems to be a non-factor in this balance, as the vertical transport drives the removal of potential temperature from the layer. More surprisingly, the tendency of the potential-temperature variance is negligible, despite the transitional nature of the event. As a result, the observed balance was reduced to

$$
-\frac{d}{dz}\overline{w'\theta'^2} \simeq -\frac{2L_v}{\rho C_p}\frac{d}{dz}\overline{\theta'\left(w'\rho'_v\right)'} - 2\overline{w'\theta'}\frac{d\overline{\theta}}{dz}. \tag{19}
$$

The production term is a dominant factor within the balance mainly at 0300 UTC, 2 h after the formation of the fog layer (0100 UTC), and is balanced by the turbulence transport. Here, no saturation processes are involved. If we exclude the 0300 UTC episode, the balance at the other peaks in the time series is governed by a balance between turbulence transport and water-vapour phase change, namely

$$
-\frac{d}{dz}\overline{w'\theta'^2} \simeq -\frac{2L_v}{\rho C_p}\frac{d}{dz}\overline{\theta'\left(w'\rho'_v\right)'}. \tag{20}
$$

Five peaks are evident at 0300, 0600, 0730, and 0830 UTC, plus a small one at 0930 UTC, three of which are given by the balance between turbulence transport and phase change.

In the remainder of this section, we analyze the spectral properties of the variances and covariances of these peaks. We consider "peak spectra" those where the 30-min time window over which the spectrum is computed
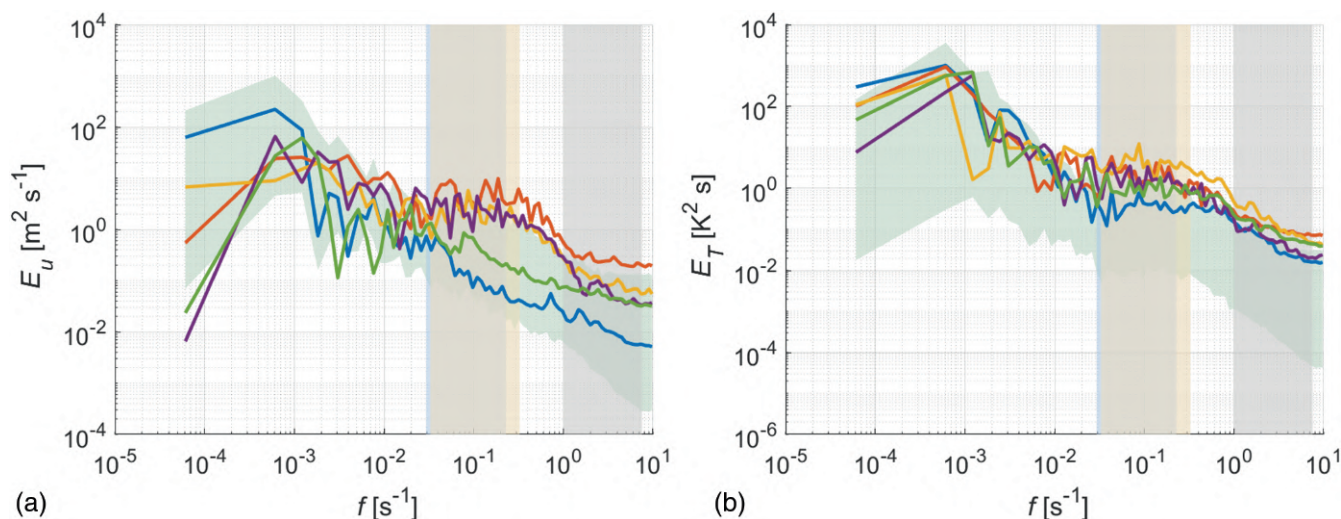
FIGURE 9 Spectra of (a) streamwise velocity and (b) potential-temperature variance as a function of frequency for the time windows of the budget peaks (solid lines: blue at 0300 UTC, red at 0600 UTC, yellow at 0730 UTC, purple at 0830 UTC, green at 0930 UTC, respectively) from Figure 8. The green shadowing area following the spectral shape is the fog-period envelope, while vertical bands describe the variability of Ozmidov (blue), Corrsin (yellow), and Taylor (grey) scales within the fog period. [Colour figure can be viewed at wileyonlinelibrary.com]

embeds one of the aforementioned peaks. We instead name as "fog-period envelope" the range identified by the minimum and maximum values at each frequency of the remaining spectra over the fog period (i.e., the period of visibility smaller than 1 km in Figure 8), computed avoiding the time windows containing the peaks. All the spectra are calculated as described in Section 3.2. Figures 9 and 10 show the spectra of relevant variances ($u'u'$ and θ'^2) and covariances ($w'u'$, $w'\theta'$, $w'\rho_v'$, and $(w'\rho_v')'$) for the budget.

We note that, despite strong peaks in the budget, the spectral quantities are similar to those typically observed in clear-sky conditions. Indeed, avoiding the peaks, the fog-period envelopes in Figure 9 resemble the common behaviour during clear-sky days, with an oscillating mean part at low frequencies and an inertial subrange. The absence of a spectral gap between them suggests the existence of a transport across scales of motion continuously altering the local equilibrium (Barbano *et al.*, 2022), which is never achieved. Considering the streamwise wind component spectrum (Figure 9a) at the peaks, we can distinguish between signals involving energy releases due to water-vapour phase change (at 0600, 0730, and 0830 UTC) and those whose balance also involve the production term (0300 and 0930 UTC). The seconds are aligned with the fog-period envelope, without displaying any discrepancies from a streamwise spectrum of a non-peak interval. When the water-vapour phase change and turbulent transport terms balance, a larger amount of turbulence energy is generated along the streamline with respect to the envelope. This characteristic is also observed in the cross-stream and vertical variances, although not shown, as the spectra are similar to the streamwise component.

Therefore, during periods when the two-term balance dominates, an increase in TKE is observed, in agreement with MacDonald *et al.* (2020), who simulated flow streaks having different moisture content, liquid content, and TKE. Conversely, the potential-temperature spectrum (Figure 9b) does not follow this distinction, as all peaks involve a heat (and so temperature and energy) exchange. Nevertheless, it is worth noticing that the amount of energy involved in the phase-change processes is typically largest during the fog period.

While the spectra show that the energy is largely contained in the inertial subrange (at the Corrsin–Ozmidov scale) and is therefore associated with turbulence, the cospectra highlight the important contribution of large-scale transport, dominant over the inertial subrange for sensible heat and water-vapour density (see Figure 10b,c). When the balance between turbulence transport and water-vapour phase change is achieved, momentum and buoyancy covariances are large, in agreement with a possible momentum divergence/convergence due to the transport. This aspect validates the fog-formation scheme highlighted in Section 4.2, with the stratus-cloud lowering towards the surface and forcing a mean energy transfer toward the ground. It also suggests that cloud lowering and associated mean energy and momentum transport are not the main drivers of turbulence production. Covariances in Figure 10a,b are almost negligible in the inertial subrange, while being maxima at lower frequencies ($f < f_O$ and/or $f < f_C$), in line with a vertical transport that is more closely associated with the scales of the mean motion rather than turbulence. Instead variances and the water-vapour phase-change
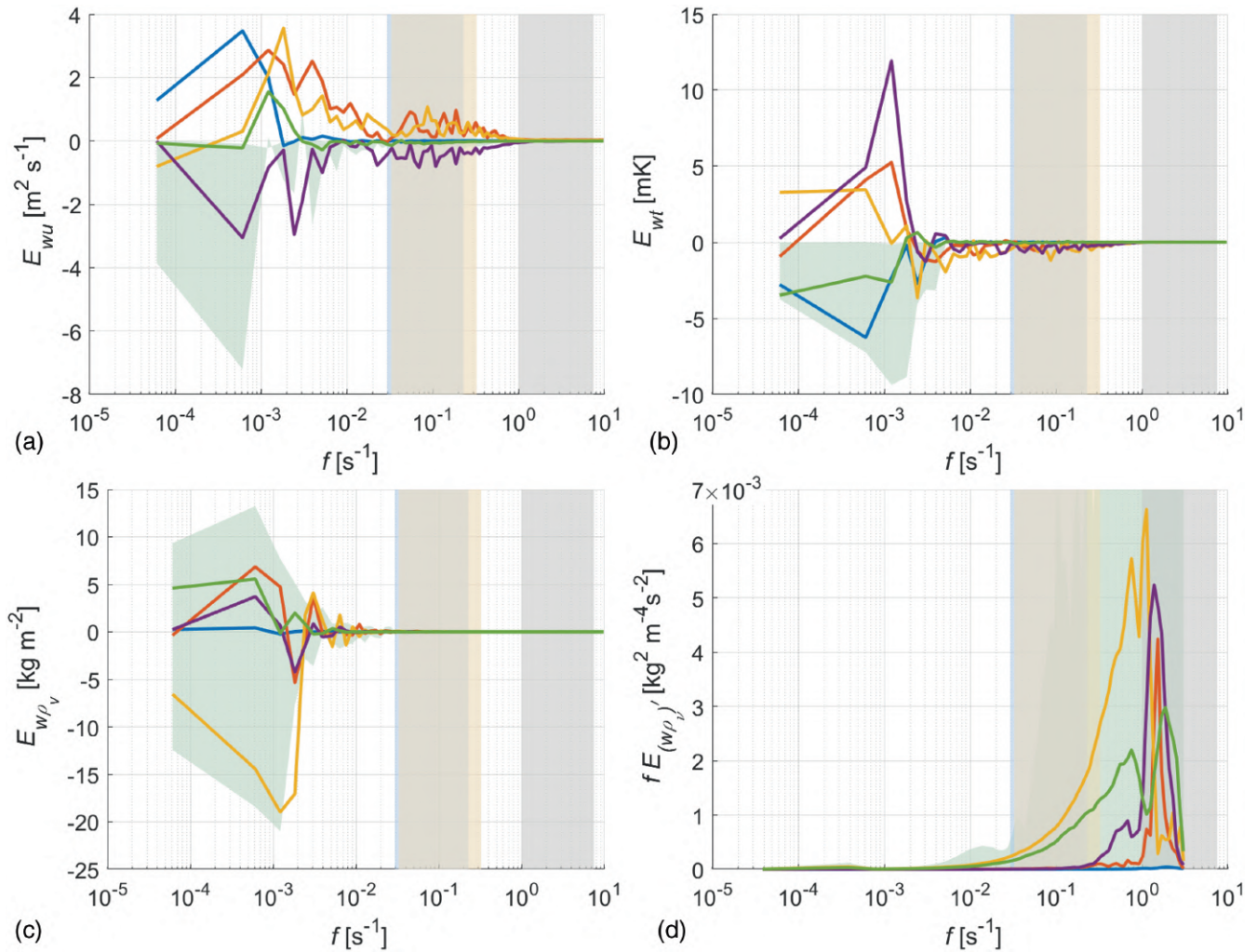
FIGURE 10 Spectra of (a) momentum, (b) buoyancy, (c) water vapour, and (d) water-vapour phase-change covariances as a function of frequency for the time windows of the budget peaks (solid lines: blue at 0300 UTC, red at 0600 UTC, yellow at 0730 UTC, purple at 0830 UTC, green at 0930 UTC, respectively) from Figure 8. The water-vapour phase-change covariance is displayed multiplied by the frequency to highlight the high-frequency range where the covariance is active. The green shadowing area following the spectral shape is the fog-period envelope, while vertical bands describe the variability of Ozmidov (blue), Corrsin (yellow), and Taylor (grey) scales within the fog period. [Colour figure can be viewed at wileyonlinelibrary.com]

term $(w'\rho_v')'$ operate at frequencies associated with the inertial subrange and the Taylor scale, suggesting the turbulence source (and sink) to be locally driven. A smaller contribution at the Corrsin–Ozmidov scale is shown in the momentum and (less so) buoyancy cospectra (see Figure 10a,b). Water-vapour processes split their contributions in both high (Corrsin–Ozmidov to Taylor scales, Figure 10d) and low (large-scale pattern, Figure 10c) frequencies. The latent heat covariance $w'\rho_v'$ (Figure 10c) involves the cloud stratus broadening towards the surface and becoming the fog layer already observed in Figure 7. The water-vapour phase change $(w'\rho_v')'$ is associated with turbulent processes within the fog layer and causes budget variability at high frequencies (see Figure 10d).

5.2 | Characterization of the potential-temperature variance transport

Since transport is a third-order moment (TOM), it is typically neglected, especially under neutral and stable conditions, where steady-state and equilibrium conditions are more likely reached (Barbano *et al.*, 2022). However, TOMs cannot be neglected a priori when these two conditions are not met. Within the convective boundary layer (CBL), TOM becomes an important factor, as the radiative heating produces turbulent mixing that is essentially non-local, resulting from the presence of large-scale semi-organized coherent structures and sustained by transport (Abdella & Petersen, 2000). In this context, the third-order moments are not negligible, but can be downscaled to second-order
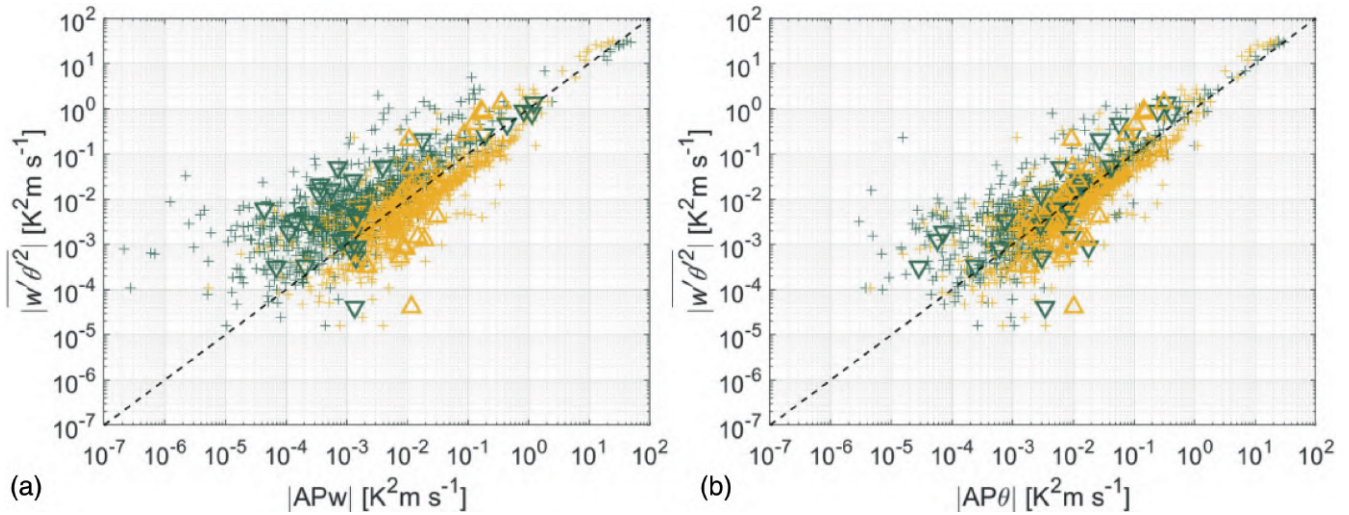
FIGURE 11 TOM as a function of its parametrizations using second-order functions of (a) the vertical velocity (Equations (21) in green and (23) in yellow) and (b) the potential temperature (Equations (22) in green and (24) in yellow). Crosses identify 1-min averages, and triangles and nablas are the 30-min averages. The black dashed line is the bisector. Data refer to the fog sub-period, 0000–1400 UTC on September 29. [Colour figure can be viewed at wileyonlinelibrary.com]

moments and then parametrized. While Abdella and Petersen (2000) show the limitations of the parametrizations in the CBL, we can still adopt their downscaling to address the TOM with an easier representation, which reads

$$\overline{w'\theta'^2} = \frac{\overline{w'^3}}{\overline{w'^2}^{3/2}} \overline{\theta'^2}^{1/2} \overline{w'\theta'}, \qquad (21)$$

or alternatively

$$\overline{w\theta'^2} = \frac{\overline{\theta'^3}}{\overline{\theta'^2}^{3/2}} \overline{\theta'^2}^{1/2} \overline{w'\theta'}. \qquad (22)$$

By using this approach, we are assuming that, under unsteady and disequilibrium conditions, the TOM behaviour converges reasonably to that observed in a CBL. Both Equations (21) and (22) can be parametrized further considering that $Sk_w = \overline{w'^3}/\overline{w'^2}^{3/2}$ and $Sk_\theta = \overline{\theta'^3}/\overline{\theta'^2}^{3/2}$ are the skewness of the vertical velocity and potential temperature, respectively, and $\sigma_\theta^2 = \overline{\theta'^2}$ is the potential-temperature variance. This gives new parametrizations based on the assumption that vertical velocities and potential temperature follow a skew-normal distribution:

$$\overline{w'\theta'^2} = Sk_w \sigma_\theta \overline{w'\theta'} = APw, \qquad (23)$$

$$\overline{w'\theta'^2} = Sk_\theta \sigma_\theta \overline{w'\theta'} = AP\theta. \qquad (24)$$

All four parametrizations provide a good representation of the TOM (Figure 11).

As expected, the skewness–variance ratio seems to be the driver of the TOM, since the second-order moment remains almost unaltered during the intermittent events. However, the second-order moment determines whether the turbulence transport is important or negligible. Using Abdella and Petersen (2000) parametrizations, $AP\theta$ shows a slightly better performance than APw. This differential is less impacting when Equations (23) and (24) are used, as Sk_w and Sk_θ are mostly similar (on average $Sk_w = Sk_\theta = 2.9$–$3\,\mathrm{m}^3{\cdot}\mathrm{s}^{-3}$).

Possible further scaling of the TOM may then depend on the Brunt–Väisälä frequency N and the skewness-to-cube-variance ratio Sk_w/σ_w^3. However, there is no evidence of a flux-gradient relation in the data (at least regarding θ), so this first hypothesis is rejected. The kinematic heat flux $\overline{w'\theta'}$ can be written in terms of the sensible heat flux H_S as

$$\overline{w'\theta'} = \frac{H_S}{\rho C_p}. \qquad (25)$$

If the most energetic peaks in the potential-temperature variance transport are associated with the water-vapour phase change, $\overline{w'\theta'^2}$ can be addressed in terms of heat flux induced by an injection of heat (corresponding to a temperature variation) due to the phase change (H_{WV}). In other words, condensation provides energy to the saturated environment, which is then transported as sensible heat. Using the aerodynamic formulation of the sensible heat flux (Lhomme *et al.*, 1988) and considering the water-vapour effect only, we obtain

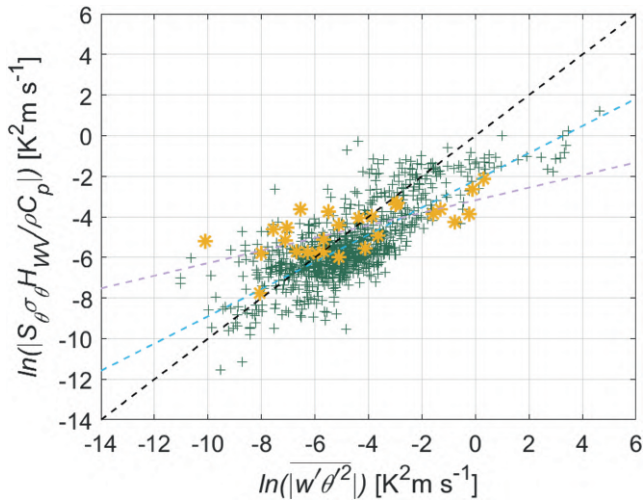$$H_{WV} = -\rho_v C_p^v \frac{T_{WV} - T}{r}, \qquad (26)$$

FIGURE 12 Parametrization of the TOM using the first-order function from Equation (28). 1-min averages are displayed with green crosses and fitted linearly using Equation (29) (dashed light blue); 30-min averages are yellow dots, fitted linearly using Equation (30) (dashed violet). The black dashed line is the bisector. Data refer to the fog sub-period, 0000–1400 UTC on September 29. [Colour figure can be viewed at wileyonlinelibrary.com]
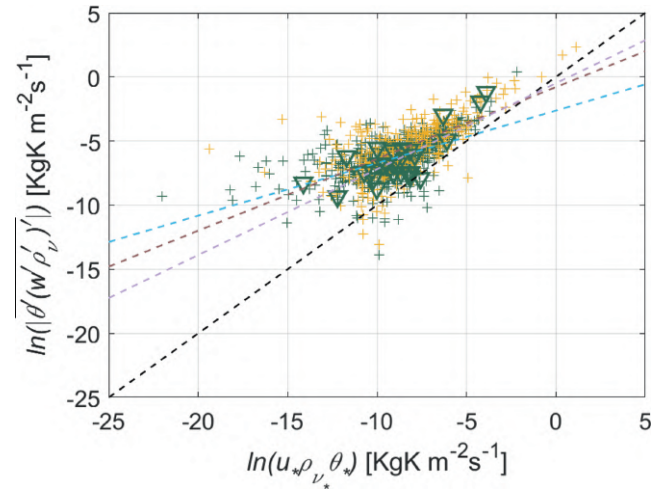

FIGURE 13 Water-vapour phase change flux $\overline{\theta'(w'\rho_v')'}$ as a function of MOST parameter, following Equation (31). 1-min averages under near-neutral (green crosses) and stable (yellow crosses) conditions are linearly fitted (considering both data samples) using Equations (32) (dashed light blue) and (33) (dashed brown); 30-min averages under near-neutral conditions are shown with green nablas, linearly fitted using Equation (34) (dashed violet). Using 30-min averages, no data under stable conditions are observed. The black dashed line is the bisector. Data refer to the fog sub-period, 0000–1400 UTC on September 29. [Colour figure can be viewed at wileyonlinelibrary.com]

where $r = U/u_*^2$ is the aerodynamic resistance modulating the heat transfer in the fog layer, $T_{WV} = e/\rho_v R_v$ is the temperature of the water vapour, T is the atmospheric temperature, ρ_v is the water-vapour density, and $C_p^v = 1940\,\mathrm{J\cdot kg^{-1}\cdot K^{-1}}$ is the specific heat at constant pressure of the water vapour. Assuming that the sensible heat is given entirely by the water-phase transformation, $H_S = H_{WV}$ and Equation (25) becomes

$$\overline{w'\theta'} = -\left(\rho_v C_p^v \frac{T_{WV} - T}{r}\right)/\rho C_p. \qquad (27)$$

Substituting Equation (27) into (24), we obtain a bulk formulation of the third-order moment that reads

$$\overline{w'\theta'^2} = -Sk_\theta\sigma_\theta\left(\rho_v C_p^v \frac{T_{WV} - T}{r}\right)/\rho C_p = Sk_\theta\sigma_\theta\frac{H_{WV}}{\rho C_p}. \qquad (28)$$

Figure 12 shows the performance of Equation (28) using the present dataset.

A best linear fit of the data shown in Figure 12 yields the following relation between the water-vapour heat flux H_{WV} and the TOM for both 1-min and 30-min averages:

$$\ln\left(|Sk_\theta\sigma_\theta H_{WV}/\rho C_p|\right)_{1\,\min}$$
$$= 0.67\ln\left(|\overline{w'\theta'^2}|\right)_{1\,\min} - 2.20, \quad R^2 = 0.60, \qquad (29)$$
$$\ln\left(|Sk_\theta\sigma_\theta H_{WV}/\rho C_p|\right)_{30\,\min}$$
$$= 0.31\ln\left(|\overline{w'\theta'^2}|\right)_{30\,\min} - 3.18, \quad R^2 = 0.48. \qquad (30)$$

The coefficients of determination R^2 are also reported. The better performance obtained using 1-min averages suggests the scale of the efficacy of TOM is shifted towards the high-frequency range of motion, in agreement with the spectral analysis within Section 3.2.

5.3 | Characterization of the water-vapour phase change

The behaviour of the water-vapour phase-change term of the modified potential-temperature budget is explored to evaluate a parametrization similar to the TOM. Being driven by (higher-order) turbulence variables, a scaling based on MOST can in principle apply within the surface layer. Scaling the water-vapour phase change using the friction velocity u_*, the potential temperature θ_* and vapour density ρ_{v*} scales, we obtain

$$\overline{\theta'(w'\rho_v')'} \propto \theta_* u_* \rho_{v*} = \frac{|\overline{w'\rho_v'}|}{u_*}u_*\theta_*. \qquad (31)$$

The MOST-based scaling underestimates the phase-change term but captures the overall data distribution

regardless of the stability condition within the fog layer or the averaging window (see Figure 13).

The water-vapour phase-change term may parametrized as a function of the MOST-based scaling through an empirical linear fit using both 1-min and 30-min averages and separating the dataset depending on stability:

$$\ln \left(\overline{|\theta'\left(w'\rho'_v\right)'|} \right)_{1\,\mathrm{min}}^{\mathrm{near\text{-}neutral}}$$

$$= 0.41 \ln \left(\theta_* u_* \rho_{v*}\right)_{1\,\mathrm{min}}^{\mathrm{near\text{-}neutral}} - 2.62, \quad R^2 = 0.34, \quad (32)$$

$$\ln \left(\overline{|\theta'\left(w'\rho'_v\right)'|} \right)_{1\,\mathrm{min}}^{\mathrm{stable}}$$

$$= 0.56 \ln \left(\theta_* u_* \rho_{v*}\right)_{1\,\mathrm{min}}^{\mathrm{stable}} - 0.79, \quad R^2 = 0.44, \quad (33)$$

$$\ln \left(\overline{|\theta'\left(w'\rho'_v\right)'|} \right)_{30\,\mathrm{min}}^{\mathrm{near\text{-}neutral}}$$

$$= 0.67 \ln \left(\theta_* u_* \rho_{v*}\right)_{30\,\mathrm{min}}^{\mathrm{near\text{-}neutral}} - 0.49, \quad R^2 = 0.59. \quad (34)$$

The coefficient of determination R^2 is also reported. Note that, when using 30-min averages, only data under near-neutral conditions are observed. Considering the 1-min averages, stability seems to be a non-dominant factor in the overall data distribution of Figure 13. It can play a role below $-10\,\mathrm{kg\cdot K\cdot m^{-2}\cdot s^{-1}}$, with the possible formation of two regimes in the flow, which can be better appreciated using a smaller averaging interval (e.g., 1 min) and subdividing the data sample by class of stability (using the local value of z/L). Addressing data under near-neutral stability, constant values of $\overline{\theta'\left(w'\rho'_v\right)'}$ are observed when the starred variables are smaller than $-10\,\mathrm{kg\cdot K\cdot m^{-2}\cdot s^{-1}}$. Conversely, stable conditions drive a decrease in the values of the water-vapour phase change at constant starred variables. Nevertheless, these observations are incomplete and possibly driven by the scarcity of data below the aforementioned threshold. Further investigation is required to confirm or dismiss our observations, which are here presented as suggested behaviours. We also explored a possible stability scaling of the form

$$\frac{\overline{|\theta'\left(w'\rho'_v\right)'|}}{\theta_* u_* \rho_{v*}} = \phi_{\mathrm{WV}}(z/L). \quad (35)$$

However, a function $\phi_{\mathrm{WV}}(z/L)$ has not been found for any stability class. Nevertheless, we note that, under near-neutral conditions, $\phi_{\mathrm{WV}}(z/L)$ increases rapidly going toward $z/L = 0$, as observed for the potential-temperature variance.
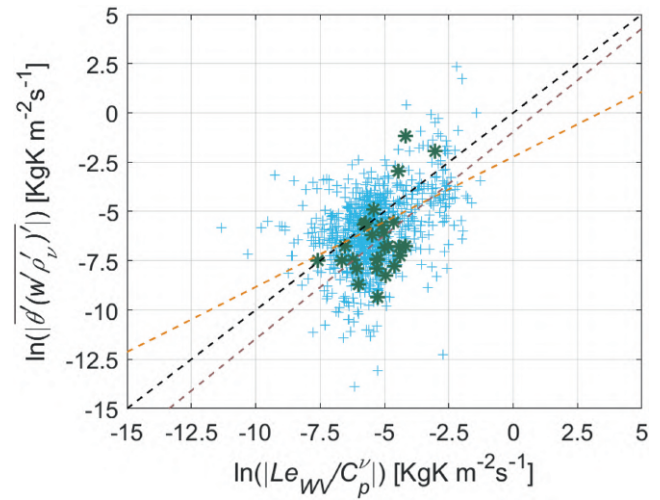

FIGURE 14 Parametrization of the water-vapour phase change flux using the first-order function from Equation (37). 1-min averages are displayed with blue crosses; 30-min averages are shown as green dots. Fits from Equations (38) and (39) are given as dashed orange and brown lines respectively for 1-min and 30-min averages. The black dashed line is the bisector. Data refer to the fog sub-period, 0000–1400 UTC on September 29. [Colour figure can be viewed at wileyonlinelibrary.com]

Similar to the potential-temperature variance transport, we try to evaluate the effect of the water-vapour phase change in terms of latent heat loss following the analogy between the kinematic water-vapour flux and the latent heat. From a bulk perspective, we are indeed assuming the heat injection/removal caused by the water-vapour phase change is governed by the energy released/absorbed by moist particles at a different partial pressure of water vapour. Using the Lhomme *et al.* (1988) formulation again, the latent heat can be written in its aerodynamic form as

$$Le_{\mathrm{WV}} = \frac{\rho_v C_{\mathrm{p}}^v}{\gamma} \frac{e_{\mathrm{s}} - e}{r}, \quad (36)$$

where the aerodynamic resistance $r = U/u_*^2$ modulates the energy exchanges in the fog layer, the psychrometric constant $\gamma = c_{\mathrm{p}} P / L_v \epsilon \simeq 66.5\,\mathrm{Pa\cdot K^{-1}}$ (with P surface pressure, L_v the latent heat of vaporization, and $\epsilon = 0.622$), e and e_{s} are the water-vapour partial pressure and its value at saturation, respectively, computed using Equations (17) and (16), ρ_v is the water-vapour density, and $C_{\mathrm{p}}^v = 1940\,\mathrm{J\cdot kg^{-1}\cdot K^{-1}}$ is the specific heat at constant pressure of water vapour. From dimensional analysis, we can rewrite the water-vapour phase change as

$$\overline{\theta'\left(w'\rho'_v\right)'} = -\frac{Le_{\mathrm{WV}}}{C_{\mathrm{p}}^v}. \quad (37)$$

The minus sign comes from the comparison between the two quantities using data averaged over 30 min. Figure 14 shows the relationship of the left-hand side of Equation (37) as a function of the right-hand side, both taken in absolute value and displaying 1-min and 30-min averaged datasets.

The correlation is addressed through the following fits:

$$\ln\left(\overline{|\theta'(w'\rho_v')'|}\right)_{1\,\mathrm{min}} = 0.66\ln\left(\left|\frac{Le_{\mathrm{WV}}}{C_p^v}\right|\right)_{1\,\mathrm{min}}$$
$$- 2.23, \quad R^2 = 0.36, \qquad (38)$$

$$\ln\left(\overline{|\theta'(w'\rho_v')'|}\right)_{30\,\mathrm{min}} = 1.05\ln\left(\left|\frac{Le_{\mathrm{WV}}}{C_p^v}\right|\right)_{30\,\mathrm{min}}$$
$$- 0.97, \quad R^2 = 0.39. \qquad (39)$$

No consistent differences have been observed using different possible fits involving function signs and/or stability. The coefficients of determination are in line with those observed for the MOST scaling, with the data distribution for different averaging times resembling the behaviour observed in Figure 13, with a double-tail tendency below $10^{-2}\,\mathrm{kg}\cdot°\mathrm{C}\cdot\mathrm{m}^{-2}\cdot\mathrm{s}^{-1}$. The bulk quantity can capture the overall phase-change behaviour.

5.4 | Length scale of water-vapour phase change

To explore the TOM–phase change balance achieved in Equation (20) further, we compare the bulk formulations for the water-vapour phase change (Equation 37) and heat transport (Equation 28). The ratio of these terms and their respective bulk formulations gives

$$\frac{\overline{w'\theta'^2}}{\frac{2L_v}{\rho C_p}\overline{\theta'(w'\rho_v')'}} = \frac{-\frac{Sk_\theta\sigma_\theta H_{\mathrm{WV}}}{\rho C_p}}{\frac{2L_v}{\rho C_p}\frac{Le_{\mathrm{WV}}}{C_p^v}} = -\frac{Sk_\theta\sigma_\theta H_{\mathrm{WV}}}{2L_v\frac{Le_{\mathrm{WV}}}{C_p^v}}$$
$$= -\frac{Sk_\theta C_p^v}{2L_v}\frac{\sigma_\theta H_{\mathrm{WV}}}{Le_{\mathrm{WV}}} \simeq -c_1\frac{\sigma_\theta H_{\mathrm{WV}}}{Le_{\mathrm{WV}}}, \qquad (40)$$

and also

$$\frac{\overline{w'\theta'^2}}{\frac{2L_v}{\rho C_p}\overline{\theta'(w'\rho_v')'}} = -\frac{Sk_\theta C_p^v}{2L_v}\frac{\sigma_\theta H_{\mathrm{WV}}}{Le_{\mathrm{WV}}}$$
$$= -\frac{Sk_\theta C_p^v}{2L_v}\frac{\sigma_\theta\left(-\rho_v C_p^v\frac{T_{\mathrm{WV}}-T}{r}\right)}{\frac{\rho_v C_p^v}{\gamma}\frac{e_s-e}{r}}$$
$$= -\frac{Sk_\theta C_p^v\gamma}{2L_v}\frac{T-T_{\mathrm{WV}}}{e_s-e} \simeq c_2\frac{\sigma_\theta(T-T_{\mathrm{WV}})}{e_s-e}, \qquad (41)$$

with $c_1 = Sk_\theta C_p^v/2L_v$ and $c_2 = Sk_\theta C_p^v\gamma/2L_v$. Considering the mean values during the fog period, $Sk_\theta C_p^v/2L_v = 1.03$ and $Sk_\theta C_p^v\gamma/2L_v = 0.07$. To check the consistency of these values, c_1 and c_2 are evaluated as constant slopes of the linear fit of the 1-min data in Figure 15. From the linear fits, $c_1 = 0.86$ and $c_2 = 0.07$ are in good agreement with the mean-value computation and also in line with the constant slopes computed from the 30-min data. For simplicity, fits in Figure 15 are computed using the mean values from Equations (40) and (41).

Both bulk formulation ratios display a widespread distribution around the expected trends, regardless of the averaging time. Mean discrepancies from the expected trends are consistent with those observed for the water-vapour phase-change parametrization only (see Figure 14), which are propagated in the balance as expected. The resulting coefficients of determination are indeed very poor (R^2 values are both close to 0.15), as the joint correlation between all terms in Equations (40) and (41) is affected by the large combined fluctuations of both turbulence covariances not being matched by the bulk quantities. It is worth noting that this evaluation still provides a qualitative interpretation of the results: both ratios can be interpreted as a higher-order Bowen ratio, where the sensible and latent heat fluxes are replaced by the turbulent transport terms. This is consistent with viewing the water-vapour phase change as a turbulent transport of heat between a saturated particle and the ambient air.

To evaluate the existence and performance of possible length-scales, we compare the terms in the potential-temperature variance equation and the respective scale quantities by means of the dimensional analysis, so that

$$\frac{d}{dz}\overline{w'\theta'^2} \sim \frac{Sk_\theta\sigma_\theta\frac{H_{\mathrm{WV}}}{\rho C_p}}{L_1} \rightarrow L_1 = \frac{Sk_\theta\sigma_\theta\frac{H_{\mathrm{WV}}}{\rho C_p}}{\frac{d}{dz}\overline{w'\theta'^2}}, \qquad (42)$$

$$\frac{2L_v}{\rho C_p}\frac{d}{dz}\overline{\theta'(w'\rho_v')'} \sim \frac{2L_v\frac{Le_{\mathrm{WV}}}{C_p^v}}{\rho C_p L_2} \rightarrow L_2 = \frac{Le_{\mathrm{WV}}}{C_p^v\frac{d}{dz}\overline{\theta'(w'\rho_v')'}}. \qquad (43)$$

Figure 16 displays a comparison between the numerator and denominator of Equations (42) and (43).

In Figure 16, linear fits computed from data with both 30-min and 1-min averaging windows are also shown. They read

$$\left(\left|\frac{d}{dz}\overline{w'\theta'^2}\right|\right)_{\mathrm{Eq.\,(42)}}^{1\,\mathrm{min}} = 0.80\ln\left(\left(Sk_\theta\sigma_\theta\frac{H_{\mathrm{WV}}}{\rho C_p}\right)_{\mathrm{Eq.\,(42)}}^{1\,\mathrm{min}}\right)$$
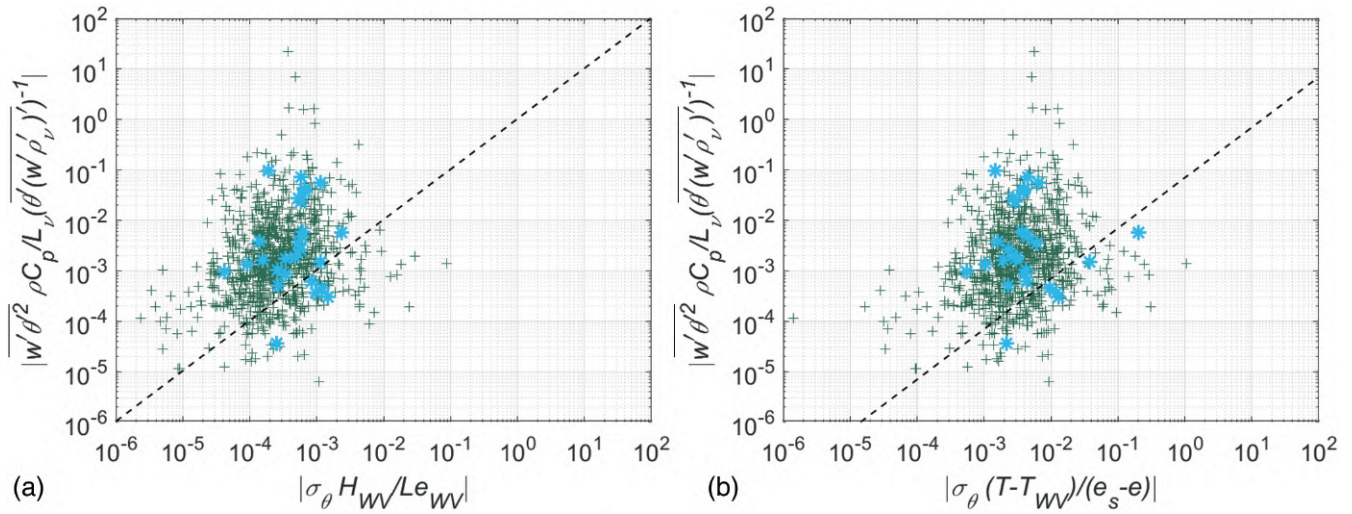$$- 0.59\ln(10), \qquad R^2 = 0.76, \qquad (44)$$

FIGURE 15 TOM water-vapour phase-change flux ratio as a function of first-order parametrizations and fits from (a) Equation (40) and (b) Equation (41). 1-min averages are displayed with blue crosses; 30-min averages are displayed with green dots. The linear fits have imposed intercepts equal to zero and slope $Sk_\theta C_p^v/2L_v = 1.03$ and $Sk_\theta C_p^v \gamma/2L_v = 0.07$, respectively. Data refer to the fog sub-period, 0000–1400 UTC on September 29. [Colour figure can be viewed at wileyonlinelibrary.com]
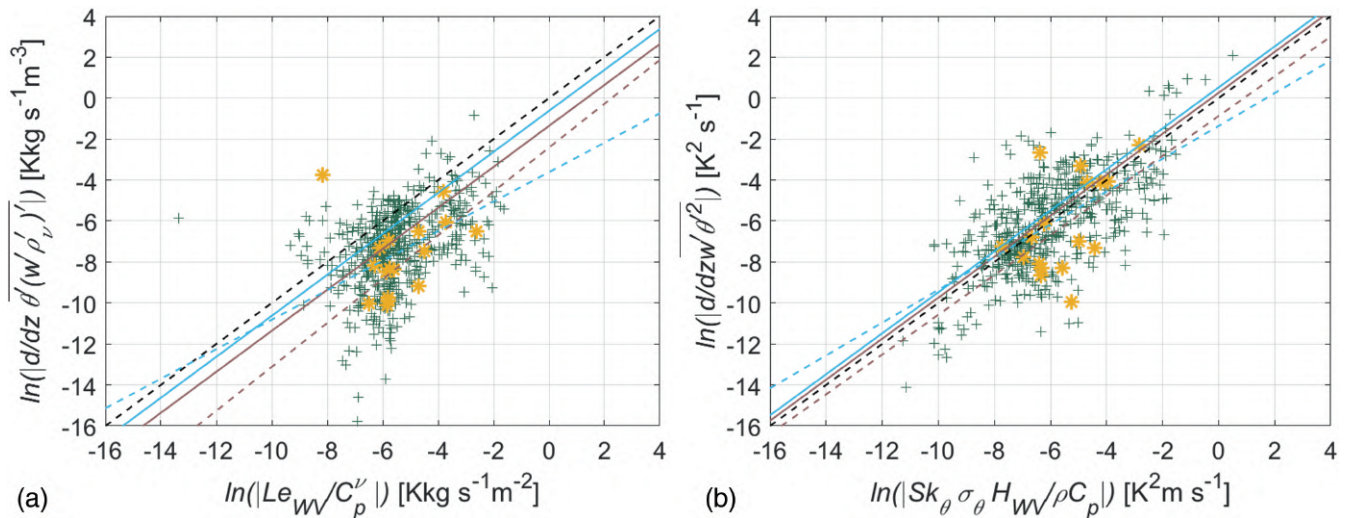

FIGURE 16 Comparison between terms of the ratios from (a) Equation (42) and (b) Equation (43). 1-min averages are displayed with green crosses; 30-min averages are displayed with yellow dots. Linear fits are computed from both 1-min (dashed light blue) and 30-min (dashed brown) averages according to Equations (46) and (47) for panel (a), Equations (44) and (45) for panel (b). Solid light blue and brown lines are built using the average values of $\langle L_1 \rangle$ and $\langle L_2 \rangle$ within the fog period as computed from 1-min and 30-min averages, respectively, according to Equation (48). The black dashed line is the bisector. Data refer to the fog sub-period, 0000–1400 UTC on September 29. [Colour figure can be viewed at wileyonlinelibrary.com]

$$\left(\left| \frac{d}{dz} \overline{w'\theta'^2} \right| \right)^{30\,min}_{Eq.\,(42)} = 0.97 \ln\left(\left(Sk_\theta \sigma_\theta \frac{H_{WV}}{\rho C_p} \right)^{30\,min}_{Eq.\,(42)} \right)$$

$$- 0.38 \ln(10), \qquad R^2 = 0.56, \qquad (45)$$

$$\left(\left| \frac{d}{dz} \overline{\theta'(w'\rho_v')} \right| \right)^{1\,min}_{Eq.\,(43)} = 0.72 \ln\left(\left(\frac{Le_{WV}}{C_p^v} \right)^{1\,min}_{Eq.\,(43)} \right)$$

$$- 1.57 \ln(10), \qquad R^2 = 0.57, \qquad (46)$$

$$\left(\left| \frac{d}{dz} \overline{\theta'(w'\rho_v')} \right| \right)^{30\,min}_{Eq.\,(43)} = 1.07 \ln\left(\left(\frac{Le_{WV}}{C_p^v} \right)^{30\,min}_{Eq.\,(43)} \right)$$

$$- 1.05 \ln(10), \qquad R^2 = 0.35. \qquad (47)$$

The fits provide a reasonable approximation of these ratios, suggesting the existence of the proposed scaling. The better correlations between 1-min covariances and respective bulk quantities reflect the impulsive nature of the

observed phenomenon, but ensure a reasonable interpretation in terms of mean quantities. In the specific case of the Equation (42) ratio, fits are consistent through the adopted averaging windows, implying the existence of a constant length-scale regardless of the average period selected (see Figure 16b). In contrast, fits in Equations (47) and (46) differ consistently from what we already observed addressing the MOST fits in Equations (32) and (34) (see Figure 16a). The difference between turbulence transport and phase-change behaviours is ascribed to the physical properties of the two quantities. Turbulence transport is intensive, as it is an intrinsic property of turbulence depending on the thermodynamic characteristic of the air and not on its volume. Conversely, phase-change processes are extensive, as the larger the air volume under investigation (or the interval of time we integrate), the greater the chances of a phase change. As already observed, the bulk approximation can replicate the overall behaviour of the phase change, but not all of its variability. Combining the different variations we can expect from an extensive process with the inability of the bulk approximation to depict the full variance, we obtain different tendencies depending on the averaging window we observe in Figure 16b. As we are about to see, similar length-scales can be obtained despite different behaviours with the averaging window. By taking the average value of $\langle L_1 \rangle$ (from Equation 42) and $\langle L_2 \rangle$ (from Equation 43) during the fog period, we get $\langle L_1 \rangle = 0.77$ m and $\langle L_2 \rangle = 3.89$ m when 30-min averages are used, $\langle L_1 \rangle = 0.59$ m and $\langle L_2 \rangle = 1.87$ m using the 1-min averages. These values are then used to compute the linear equations,

$$y = \langle L_{1,2} \rangle x, \tag{48}$$

displayed in logarithmic form in Figure 16. Values of $\langle L_1 \rangle$ are close to the slopes of the linear fits in Equations (45) and (44), as the bulk approximation is consistently aligned to its third-order moments (despite general data that are widespread, consistent with what we already observed in Section 5.2). Conversely, a larger difference is measured for $\langle L_2 \rangle$, as expected from the linear fits in Equations (47) and (46). Nevertheless, the logarithmic form of Equation (48) shows a small discrepancy with the averaging choice and provides a reasonable trend of the phase change and its approximation, as it captures the overestimation by the bulk term with respect to the third-order moment.

From the phase-change length-scales, we retrieved the characteristic frequencies computed from 1-min and 30-min averages accordingly using Taylor's frozen-turbulence hypothesis and the mean wind speed in the layer during the fog period. We obtain $\langle \overline{F}_2 \rangle = [0.74, 1.53]$ s^{-1}, depending on the averaging windows. This range of characteristic frequencies is in line with the
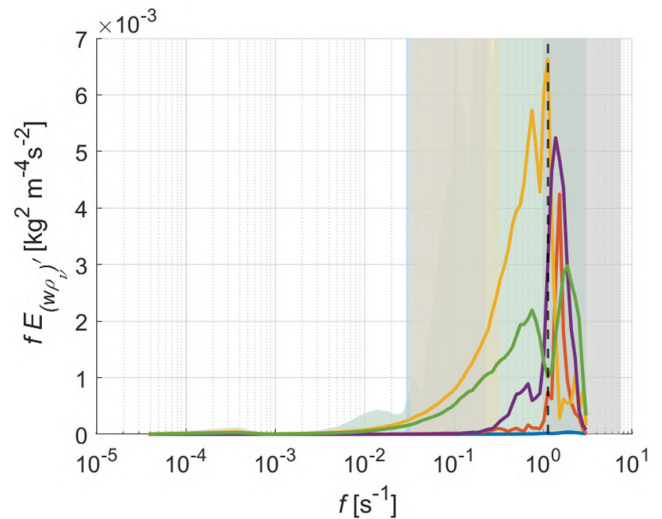

FIGURE 17 Spectra of the water-vapour phase-change covariance as a function of frequency for the time windows of the budget peaks (solid lines: blue at 0300 UTC, red at 0600 UTC, yellow at 0730 UTC, purple at 0830 UTC, green at 0930 UTC, respectively) from Figure 8. The green shadowing area following the spectral shape is the fog-period envelope, while vertical bands describe the variability of Ozmidov (blue), Corrsin (yellow), and Taylor (grey) scales within the fog period. The black vertical line is the line at the characteristic frequency $\langle \overline{F}_2 \rangle = 1.14$ s^{-1}. [Colour figure can be viewed at wileyonlinelibrary.com]

water-vapour density spectrum, plotted here once again in Figure 17.

Specifically, the average value of the frequency range $\langle \overline{F}_2 \rangle = 1.14$ s^{-1} is close to the major peaks of the spectral signals representing the potential-temperature variance budget peaks (see Figure 8). We can conclude that $\langle \overline{F}_2 \rangle$ is a reasonable estimation of the characteristic scale of the water-vapour phase-change process inferring the turbulence energy budget, despite being based only on bulk quantities (and therefore being accessible whether or not turbulence measurements are accessible). As a final note, $\langle \overline{F}_2 \rangle = 1.14$ s^{-1} stands as a cutting edge between the Taylor dissipation scale and the buoyancy-production scales, depicting the turbulent phase change as a process close to the dissipation scale but still important for the energy balance.

6 | CONCLUSIONS

Turbulence behaviour within fog remains a fascinating yet not fully understood topic. Despite being weak, its contribution to the energy balance is not negligible and depends on the characteristics of the saturated environment. In this article, we have investigated the effects of saturation processes on the potential-temperature variance budget.

We have introduced a novel term in the budget consisting of the variation of the latent heat flux and accounting for the heat exchanged by the water-vapour phase change between the saturated particles and the ambient air. We then tested the performance of the improved budget and evaluated a possible bulk scaling of the simplified balance using data from ground-based instrumentation located in the Avalon Peninsula, Newfoundland, Canada during the C-FOG Research Program. The results show that intermittent energy bursts are caused by the turbulent injection of heat in the air caused by the phase change of water vapour, and the heat excess is redistributed in the air volume through turbulent transport. In other words, potential energy production within fog is not always transferred from the mean flow, but it can originate from heat removal/injection due to the change of phase, marking the necessity of considering and evaluating the newly introduced term of the budget. The transport-to-phase-change balance obtained during the intermittent events has been explored further and bulk parametrizations of the two terms have been suggested, based on the aerodynamic formulations of the sensible and latent heat fluxes. The parametrizations capture the behaviours of the high-order terms of the balance with reasonable agreement, opening the possibility of computing the balance using bulk quantities only, which would be used in numerical weather prediction models. From the parametrizations, length-scales of the processes are evaluated, locating the phase-change processes between the buoyancy-production and Taylor scales.

Despite the case-study approach of this work, the theoretical framework, parametrizations, and length-scales can be used in other contexts of strong saturation at the surface. We are conscious that a single case study is not sufficient proof for a theory modification, but we hope that our results could inspire research related to saturation turbulence processes.

ACKNOWLEDGEMENTS

CONFLICT OF INTEREST STATEMENT

The authors declare they have no conflict of interest.

DATA AVAILABILITY STATEMENT

The data that support the findings of this study are available from the corresponding author upon reasonable request.

ORCID

Francesco Barbano https://orcid.org/0000-0002-4403-7070
Eric Pardyjak https://orcid.org/0000-0002-0180-0857

REFERENCES

Abdella, K. & Petersen, A. (2000) Third-order moment closure through a mass-flux approach. *Boundary-Layer Meteorology*, 95(2), 303–318.

Barbano, F., Brogno, L., Tampieri, F. & Di Sabatino, S. (2022) Interaction between waves and turbulence within the nocturnal boundary layer. *Boundary-Layer Meteorology*, 183(1), 35–65.

Bergot, T. (2013) Small-scale structure of radiation fog: a large-eddy simulation study. *Quarterly Journal of the Royal Meteorological Society*, 139(673), 1099–1112.

Cuxart, J., Conangla, L. & Jiménez, M. (2015) Evaluation of the surface energy budget equation with experimental data and the ECMWF model in the Ebro Valley. *Journal of Geophysical Research: Atmospheres*, 120(3), 1008–1022.

Dione, C., Haeffelin, M., Burnet, F., Lac, C., Canut, G., Delanoë, J. et al. (2023) Role of thermodynamic and turbulence processes on the fog life cycle during SOFOG3D experiment. *Atmospheric Chemistry and Physics*, 23(24), 15711–15731.

Dorman, C.E., Hoch, S.W., Gultepe, I., Wang, Q., Yamaguchi, R.T., Fernando, H. et al. (2021) Large-scale synoptic systems and fog during the C-FOG field experiment. *Boundary-Layer Meteorology*, 181(2), 171–202.

Fernando, H.J., Gultepe, I., Dorman, C., Pardyjak, E., Wang, Q., Hoch, S. et al. (2021) C-FOG: life of coastal fog. *Bulletin of the American Meteorological Society*, 102(2), E244–E272.

Grachev, A.A., Krishnamurthy, R., Fernando, H.J., Fairall, C.W., Bardoel, S.L. & Wang, S. (2021) Atmospheric turbulence measurements at a coastal zone with and without fog. *Boundary-Layer Meteorology*, 181(2), 395–422.

Grachev, A.A., Leo, L.S., Fernando, H.J., Fairall, C.W., Creegan, E., Blomquist, B.W. et al. (2018) Air-sea/land interaction in the coastal zone. *Boundary-Layer Meteorology*, 167(2), 181–210.

Gultepe, I., Tardif, R., Michaelides, S.C., Cermak, J., Bott, A., Bendix, J. et al. (2007) Fog research: a review of past achievements and future perspectives. *Pure and Applied Geophysics*, 164(6), 1121–1159.

Hang, C., Nadeau, D.F., Pardyjak, E.R. & Parlange, M.B. (2020) A comparison of near-surface potential temperature variance budgets for unstable atmospheric flows with contrasting vegetation cover flat surfaces and a gentle slope. *Environmental Fluid Mechanics*, 20(5), 1251–1279.

Hejstrup, J. (1993) A statistical data screening procedure. *Measurement Science and Technology*, 4, 153–157.

Huang, H., Liu, H., Huang, J., Mao, W. & Bi, X. (2015) Atmospheric boundary layer structure and turbulence during sea fog

on the southern China coast. *Monthly Weather Review*, 143(5), 1907–1923.

Kaimal, J.C. & Finnigan, J.J. (1994) *Atmospheric boundary layer flows: their structure and measurement*. Oxford, UK: Oxford University Press.

Kalogirou, S.A. (2009) Chapter five—Solar water heating systems. In: Kalogirou, S.A. (Ed.) *Solar energy engineering*. Boston, MA: Academic Press, pp. 251–314.

Koračin, D., Businger, J.A., Dorman, C. & Lewis, J.M. (2005) Formation, evolution, and dissipation of coastal sea fog. *Boundary-Layer Meteorology*, 117, 447–478.

Koračin, D., Dorman, C.E., Lewis, J.M., Hudson, J.G., Wilcox, E.M. & Torregrosa, A. (2014) Marine fog: a review. *Atmospheric Research*, 143, 142–175.

Lewis, J., Koračin, D. & Redmond, K. (2004) Sea fog research in the United Kingdom and United States: a historical essay including outlook. *Bulletin of the American Meteorological Society*, 85(3), 395–408.

Lhomme, J.P., Katerji, N., Perrier, A. & Bertolini, J.M. (1988) Radiative surface temperature and convective flux calculation over crop canopies. *Boundary-Layer Meteorology*, 43(4), 383–392.

MacDonald, M., Kurowski, M.J. & Teixeira, J. (2020) Direct numerical simulation of the moist stably stratified surface layer: turbulence and fog formation. *Boundary-Layer Meteorology*, 175(3), 343–368.

Maronga, B. & Bosveld, F. (2017) Key parameters for the life cycle of nocturnal radiation fog: a comprehensive large-eddy simulation study. *Quarterly Journal of the Royal Meteorological Society*, 143(707), 2463–2480.

Nakanishi, M. (2000) Large-eddy simulation of radiation fog. *Boundary-Layer Meteorology*, 94(3), 461–493.

Oliver, D.A., Lewellen, W.S. & Williamson, G.G. (1978) The interaction between turbulent and radiative transport in the development of fog and low-level stratus. *Journal of Atmospheric Sciences*, 35(2), 301–316.

Schiavon, M., Barbano, F., Brogno, L., Leo, L.S., Tampieri, F. & Di Sabatino, S. (2003) On the parametrizations for the dissipation rate of the turbulence kinetic energy in stable conditions. *Bulletin of Atmospheric Science and Technology*, 4, 3.

Singh, D., Hoch, S., Gultepe, I. & Pardyjak, E. (2023) A case study of the life cycle of a stratus-lowering coastal-fog event in Newfoundland, CA. *Quarterly Journal of the Royal Meteorological Society*, 150(759), 641–662.

Stull, R.B. (1988) *An introduction to boundary layer meteorology*, Vol. 13. Dordrecht: Springer Science and Business Media.

Terradellas, E., Ferreres, E. & Soler, M.R. (2008) Analysis of turbulence in fog episodes. *Advances in Science and Research*, 2(1), 31–34.

Vickers, D. & Mahrt, L. (1997) Quality control and flux sampling problems for tower and aircraft data. *Journal of Atmospheric and Oceanic Technology*, 14(3), 512–526.

Wilczak, J.M., Oncley, S.P. & Stage, S.A. (2001) Sonic anemometer tilt correction algorithms. *Boundary-Layer Meteorology*, 99(1), 127–150.

Zhou, B. & Ferrier, B.S. (2008) Asymptotic analysis of equilibrium in radiation fog. *Journal of Applied Meteorology and Climatology*, 47(6), 1704–1722.